Can a coupled meteorology-chemistry model reproduce the historical trend in aerosol direct radiative effects over the northern hemisphere?

Jia Xing[1], Rohit Mathur[1], Jonathan Pleim[1], Christian Hogrefe[1], Chuen-Meei Gan[1], David C. Wong[1], Chao Wei[1, 2]

[1] The U.S. Environmental Protection Agency, Research Triangle Park, NC 27711, USA

[2] Multiphase Chemistry Department, Max Planck Institute for Chemistry, 55128 Mainz, Germany

Correspondence to: Jia Xing (xing.jia@epa.gov, xingjia@tsinghua.org.cn)

Abstract

The ability of a coupled meteorology-chemistry model, i.e., WRF-CMAQ, in reproducing the historical trend in AOD and clear-sky short-wave radiation (SWR) over the northern hemisphere has been evaluated through a comparison of 21-year simulated results with observation-derived records from 1990-2010. Six satellite retrieved AOD products including AVHRR, TOMS, SeaWiFS, MISR, MODIS-terra and –aqua as well as long-term historical records from 11 AERONET sites were used for the comparison of AOD trends. Clear-sky SWR products derived by CERES at both TOA and surface as well as surface SWR data derived from seven SURFRAD sites were used for the comparison of trends in SWR. The model successfully captured increasing AOD trends along with the corresponding increased TOA SWR (upwelling) and decreased surface SWR (downwelling) in both eastern China and the northern Pacific. The model also captured declining AOD trends along with the corresponding decreased TOA SWR (upwelling) and increased surface SWR (downwelling) in eastern U.S., Europe and northern Atlantic for the period of 2000-2010. However, the model underestimated the AOD over regions

with substantial natural dust aerosol contributions, such as the Sahara Desert, Arabian Desert, central Atlantic and north Indian Ocean. Estimates of aerosol direct radiative effect (DRE) at TOA are comparable with those derived by measurements. Compared to GCMs, the model exhibits better estimates of surface- aerosol direct radiative efficiency (E_τ). However, surface-DRE tends to be underestimated due to the underestimated AOD in land and dust regions. Further investigation of TOA-E_τ estimations as well as the dust module used for estimates of windblown- dust emissions is needed.

Keywords: aerosol direct radiation effect, WRF-CMAQ, modeling, trend, AOD, clear-sky shortwave radiation, northern hemisphere

1. Introduction

Solar radiation, the Earth's primary energy source, plays a crucial role in the climate system. The decadal variations in surface shortwave radiation (SWR) starting from 1950s and related climate impacts have been well documented (Ohmura and Wild, 2002; Mercado et al., 2009; Ohmura, 2009; Wild et al., 2005, 2007; Wild, 2009). Many studies suggest that such variations were caused by the changes in anthropogenic aerosol loading over this time period (Streets et al., 2006; Ruckstuhl and Norris, 2009; Ohmura, 2009). Atmospheric aerosols not only directly scatter or absorb solar radiation (McCormick and Ludwig, 1967), but also affect surface solar radiation indirectly by altering cloud optical properties and lifetime (Twomey, 1977; Albrecht, 1989). The global aerosol effective radiative forcing at the top of atmosphere (TOA) is estimated to have cooling effects from both aerosol-radiation interactions (-0.95 to +0.05 W m^{-2}) and aerosol-cloud interactions (-1.2 to 0.0 W m^{-2}) which are comparable in magnitude to the

warming effects by anthropogenic greenhouse gases (2.83 W m^{-2}) (IPCC 2014). However, large discrepancies in aerosol radiative forcing exist amongst the results estimated by different approaches, particularly at a regional scale. Aerosol direct radiative effects (DRE) simulated by global chemical transport models (CTMs) are 30-40% smaller than those derived from measurements (Yu et al., 2006). Additionally, decadal changes in surface SWR are considerably underestimated by Global Climate Models (GCMs) (Wild, 2009) for both clear- and all-sky conditions. For example, Ruckstuhl and Norris (2009) stated that the surface SWR trends in Europe under cloud-free conditions simulated by the IPCC-AR4 models, are smaller on average than that indicated by the observational evidence, and such large discrepancies in sign and magnitude between modeled and observed trends may be caused by large uncertainties in historic emission inventories and associated aerosol burdens. Thus to draw robust interpretations of long-term records and assessments of aerosol impacts on climate forcing, more accurate descriptions of atmospheric aerosol loading, optical properties, and spatial-temporal distribution is necessary.

A two-way coupled meteorology and atmospheric chemistry model, i.e., Weather Research and Forecast (WRF) model coupled with the Community Multiscale Air Quality (CMAQ) model, has been developed by U.S. Environmental Protection Agency (Pleim et al., 2008; Mathur et al., 2010; Wong et al., 2012; Yu et al., 2013; Mathur et al., 2014; Wang et al., 2014). This model system can be applied as an integrated regional climate and chemistry model, serving as an important tool for downscaling future projections of global climate to higher resolution as well as assessing the interactions between atmospheric chemistry, radiation, and meteorology. A preliminary analysis on a ten-day WRF-CMAQ simulation of a wildfire event in California suggests that including the radiative effects of aerosols improves the accuracy of both the meteorology and air quality simulations (Wong et al., 2012). However, an assessment of the

performance of such coupled models in reproducing the aerosol radiative effects is needed to build confidence in their use as regional climate-chemistry models over decadal time periods. Decadal hemispheric WRF-CMAQ simulations from 1990-2010 were conducted and evaluated through comparison with long-term surface observations of gaseous and particle species in our recent study (Xing et al., 2015). The current study focuses on aerosol direct radiative effects (DRE) and aims to answer the following questions: (1) How well does the new model represent the regional and temporal variability of aerosol burden and DRE?, and (2) Is the model able to capture past trends in aerosol loading and associated radiative effects?

A brief description of the model configuration and observations is given in section 2. The evaluation of the model simulated historical AOD and clear-sky SWR is presented in sections 3.1 and 3.2. The estimates of DRE are provided in section 3.3. Aerosol radiative efficiency is further discussed in section 4.

2. Method

2.1 Model configuration

This study focuses on the summer months (June, July, and August) over a 21 year period (1990-2010) using WRF-CMAQ (WRFv3.4 coupled with CMAQv5.0) driven by internally consistent historical emission inventories obtained from EDGAR. Details about emission processing and WRF configuration are described in Xing et al (2015). The strength of nudging coefficients for four dimensional data assimilation and indirect soil temperature nudging employed in WRF have been tested and chosen to improve model performance for meteorological variables without dampening the effects of radiative feedbacks. The nudging coefficient for both u/v-wind and potential temperature is set to 0.00005 sec^{-1}, while 0.00001 sec^{-}

[1] is used for nudging of water vapor mixing ratio. The simulation domain is shown in Figure 1 and covers most of the northern hemisphere, discretized with a grid of 108 km×108 km resolution and 44 vertical layers of variable thickness between the surface and 50mb (Xing et al, 2015). For further analysis and comparison with measurements we selected four sub-regions over land (including adjacent ocean areas which might be impacted by transport from land) and four sub-regions mostly over the ocean. Three of these land regions are mostly impacted by anthropogenic emissions, i.e., eastern China (ECH, 20N-40N, 100E-125E) and eastern US (EUS, 28N-50N, 100W-70W), Europe (EUR, 35N-65N, 10W-30E) while the fourth land region is largely impacted by dust emissions i.e., Sahara Desert and Arabian Desert (SHR, 10N-25N, 10W-50E). Out of the four ocean regions, the North Pacific (NPA, 30N-50N, 150E-130W) is in between ECH and EUS, the North Atlantic (NAT, 35N-50N, 60W-15W) is in between EUR and EUS, and the remaining two regions are downwind of SHR, i.e., Central Atlantic (CAT, 10N-25N, 60W-15W) and North Indian Ocean (NIN, 10N-25N, 55E-75E).

Both the feedback and non-feedback cases were simulated using the same model configuration and initial condition obtained from our previous continuous 21-year WRF-CMAQ simulations (Xing et al., 2015) except that aerosol direct radiative effects updated in the rapid radiative transfer model (RRTMG) (Clough et al., 2005) were considered in the feedback case. Similar to Hogrefe et al (2015), in the non-feedback case, no default or climatological aerosol profiles were provided to the RRTMG model employed in WRF. Therefore, there are no aerosol effects on the radiation calculations in the non-feedback case. DRE is thus estimated as the difference between feedback and non-feedback simulations. In addition, the coupled model used in this study allows the DRE to affect the dynamical fields and also represent the subsequent modulation of aerosol quantities associated with the "updated" dynamical fields, such as soil dust

emission flux and photolysis rates which are calculated online with the dynamical model.

Aerosol indirect effects by altering cloud optical properties and lifetime were not considered in current study. Efficiencies for extinction, total scattering, backscattering, and asymmetry factor for single particle were calculated using the BHCOAT coated-sphere module approach (Bohren and Huffman 1983). Aerosol effects are treated dynamically in the coupled system, where the CMAQ chemistry and radiation-feedback modules are called every 5 and 20 time steps of WRF, respectively. The time step of WRF was set to be 60 seconds in simulation, thus the meteorology fields will be updated from the feedback module every 20 minutes in simulation. Thus space and time varying aerosol optical properties estimated from simulated aerosol composition and size distribution are used in the RRTM based radiation calculations and impact the simulated dynamical and chemical state of the atmosphere.

2.2 Long-term observations

Table 1 summarizes the observation data used in this study including satellite-retrieved and surface-based measured AOD and clear-sky radiation.

2.2.1 Aerosol optical depth (AOD)

Historical satellite remote sensing of AOD has been recorded back to the 1980s. Despite limitations in accuracy (Chu et al., 2002), the satellite measured AOD has global distributions with relative long-time coverage which makes it suitable to evaluate model simulation performance (Roy et al., 2007; Liu et al., 2010; Wang et al., 2010, 2011) and to understand the evolution of atmospheric aerosols (Chin et al., 2014). To minimize the influences from uncertainties of single satellite product, we conducted our analysis based on all available satellite retrievals (or averages) with more robust estimates (e.g., level-3 dataset). The Advanced Very High Resolution Radiometer (AVHRR) provides the longest-running global satellite observations,

starting in 1981. Long-term AVHRR retrieved AOD over the oceans (AVHRR retrievals are unavailable over land due to relatively large uncertainties associated with surface reflectance over land surface) has been produced by the NOAA Climate Data Record (CDR) project (Chan et al., 2013; Zhao et al., 2013). Five satellite retrieval products which cover both land and ocean are also used in this study (Table 1). Total Ozone Mapping Spectrometer (TOMS) is one of the earliest satellites providing AOD measurement products with data from 1979 to 2001 (Torres et al., 1998; 2002). However, it's not specifically designed to measure aerosols and thus has limited accuracy (Chin et al., 2014). Both the TOMS product and AVHRR product are only used here for trend analysis. The other four data sources are more recent satellite products, i.e., the Seaviewing Wide Field-of-view Sensor (SeaWiFS) (McClain et al., 1998; Hsu et al., 2012; Sayer et al., 2012), the Multiangle Imaging Spectroradiometer (MISR) (Kahn et al., 2005; 2010) and the Moderate Resolution Imaging and Spectroradiometer (MODIS) on both NASA's Earth Observing System (EOS)-Terra and EOS-Aqua satellites (Kaufman et al., 1997; Remer et al., 2005, 2008; Levy et al., 2010) which have improved accuracy mostly covering the period of the 2000s. The bright desert surfaces which are missing in the "dark target" retrieval (ver. 5.1) in the MODIS AOD product are filled by the "deep blue" retrieval which uses the 412 nm channel of MODIS to enable the retrieval of AOD over bright surfaces over land (Hsu et al., 2004), An exception to this is for MODIS-terra data after 2007 when there is no deep-blue retrieval available.

In conducting the model-observed comparisons, the satellite datasets are interpolated to the 108 km × 108 km grid of the CMAQ northern hemispheric domain as shown in Figure 1. The grid matching was conducted by using simple inverse distance weighting method. To be consistent with the specific time that the satellite crosses the equator, especially for the four more recent satellites, i.e., MISR (10:30am local time), SeaWiFS (noon local time), MODIS-terra

(10:30am local time) and MODIS-aqua (1:30pm local time), we chose to extract the AOD from model outputs at 11:00 am (local time).

Model-simulated AOD is also compared with measurements from the worldwide ground-based Aerosol Robotic Network (AERONET) which has been widely used for satellite product validation and model evaluations because of its direct measurements and unified high standard for instrument calibration (Holben et al., 2001; Chin et al., 2014). We select eleven sites from the AERONET with relatively long-term historical records to enable comparison of AOD trends, as additional evidence demonstrating the decadal changes in the tropospheric aerosol burden. For the purpose of comparison with the model, all the AERONET AOD observations were converted to the 533nm band based on the equation of Ångström exponent.

2.2.2 Clear-sky radiation

Since this study focuses on the aerosol direct radiative effect, the clear-sky SWR product is examined in this analysis. The Clouds and the Earth's Radiant Energy System (CERES) instruments developed for NASA's EOS report observations starting in 1997 (Wielicki et al, 1996, 1998). The CERES Energy Balanced and Filled (EBAF) dataset provides satellite-derived clear-sky shortwave radiation at TOA over the globe on a monthly-averaged basis starting from 2000 (Loeb et al., 2009, 2012). Such observation-derived clear-sky SWR at TOA with global coverage is suitable for comparison with model simulations (Satheesh and Ramanathan, 2000; Rajeev and Ramanathan, 2001; Anantharaj et al., 2010) and estimation of the DRE (Yu et al., 2006; Patadia et al., 2008) at a regional scale.

Efforts have also been made to establish records of observation-derived clear-sky shortwave radiation at the surface, for the purpose of reducing the uncertainties in the fluxes at the surface which are significantly larger than those at the TOA (Wild et al., 2006). For surface

observations with high-frequency such as World Climate Research Programs Baseline Surface Radiation Network (WCRP-BSRN), it is possible to process a stratification of records into cloudy and clear-sky periods on the basis of an advanced clear-sky detection algorithm (Long et al., 2000; Wild et al., 2005) and to validate the model (Wild et al., 2006; Freidenreich and Ramaswamy et al., 2011). Unlike those at the TOA, the surface fluxes cannot be directly measured by satellites. However, the CERES mission estimates a global clear-sky surface SWR through radiative transfer calculations using satellite-retrieved surface, cloud, and aerosol properties as input (Kato et al., 2013) which agrees with the surface observations on a global mean level (Wild et al., 2013). The satellite-derived surface product has also been used in recent analyses (Hakuba et al., 2014).

For comparison with model simulations on a regional scale, we used the CERES-derived clear-sky shortwave radiations at both TOA and surface. In addition, we used clear-sky SWR at seven sites of the Surface Radiation Budget Network (SURFRAD, a component of the BSRN network) processed by Gan et al., (2014). These seven sites are grouped into the eastern U.S. (incl., Bondville, IL; Goodwin Creek, MS; Penn State, PA; Southern Great Plains, OK) and the western U.S. (incl., Table Mountain, CO; Desert Rock, NV; Fort Peck, MT) for comparison with simulations.

In consideration of the limited length of record, as in our previous study (Xing et al, 2015), this study only focuses on linear trends. The linear least square fit method was employed, and significance of trends was examined with a Student t test at the 80%, 90% and 95 % confidence levels ($p = 0.2$, 0.1 and 0.05). To be consistent with the available period of satellite products mostly covering the period of the 2000s, the two decades were separated into two time periods spanning, i.e., 1990s (1990-2010) and 2000s (2000-2010) for analysis.

3. Results

3.1 Trends in AOD

3.1.1 Comparison with satellite-retrieved AOD

Due to discrepancies in the sensitivities and retrieval algorithms of the various sensors, satellite-retrieved AODs from the different platforms are not necessarily consistent with each other. Figure 2 displays the spatial distribution of JJA-averaged AOD from multiple-platform satellite retrieval datasets as well as from the model simulation. The "polluted half-circle" which starts from Sahara Desert to East Asia is evident in MISR, MODIS-terra and –aqua. Missing data are found in large areas of China and India in both TOMS and SeaWiFS retrieved AOD. Inconsistencies among satellite-retrievals are also noticeable in the North Pacific Ocean as well as in southwest of the United States where higher AOD are shown in MODIS-terra and –aqua but low or no value in other satellite retrievals. In general, the model captures the spatial pattern of AOD but underestimates the AOD levels in dust areas including the Sahara Desert, the Arabian Desert, the Indo-Gangetic basin in the north India which is affected by dust storms coming from the west during summer (Prasad and Singh, 2007) as well as the Gobi Desert in western China. Such underestimations as well as unexpected high AOD estimates in Hawaii might be associated with the uncertainty of the wind-blown dust module in which parameters related to the calculation of "threshold friction velocity" need future investigation (Fu et al., 2014). Ridley et al. (2014) found similar underestimation of summer AOD over the Sahel in their modeling study, suggesting that such biases might be associated with the Haboobs-driven dust emission which is not well represented in current dust module (Marsham et al., 2011). However, the model captures the moderate AOD level in the east U.S. (EUS) and Europe (EUR) in early years and high AOD level in east China (ECH) where anthropogenic aerosols are the dominant contributors. Slight

underestimation in ECH and EUS might be associated with underestimation of fine particles (Xing et al., 2014) as well as poor representation of secondary organic aerosol formation is more evident in summer (see Figure 3a, b, c).

The model successfully captured AOD trends after 2000 in three non-dust land regions (i.e., ECH, EUS and EUR). The spatial distribution of AOD trend (yr^{-1}) and time series of region-averaged AOD are provided in Figure 2 and Figure 3 respectively. In ECH, significant increase in AOD level is suggested from satellite retrievals, with growth rates of +0.001 to +0.004 (+0.3 to +1.7%) yr^{-1}. Such increase of AOD has also been simulated by the model, though with a faster growth of +0.014 (+5.3%) yr^{-1} (see Table 2). The overestimation of the AOD trend in ECH is caused by the discrepancy between the simulated and observed AOD trend over the southern part of east-China which can be strongly influenced by biomass burning in Southeast Asia (Deng et al., 2008; Fu et al., 2012). As displayed in Figure 2, the model failed to capture the negative trend of the satellite retrieved AODs in the south-east Asia. Variations of biomass burning activity in Southeast Asia is difficult to capture in the model without an accurate temporally resolved biomass emission inventory, currently not available. The declining trends shown in observed AOD might be also associated with the recession since late 2008 (Lin et al., 2010) which may be not well represented in the emission inventory. The SeaWiFS retrieved AOD presents a more significant (at p=0.1 level) increasing trend compared to other satellite products, though the growth rate (+0.004 yr^{-1}) is still lower than that of simulated AOD trend (+0.014 yr^{-1}). The simulated declining trends of -0.004 (-2.7%) yr^{-1} in EUS and -0.003 (-2.1%) yr^{-1} in EUR, are very close to the observed trends of -0.003 to -0.008 (-1.5 to -4.4%) yr^{-1} and -0.002 to -0.007 (-1.0 to -3.8%) yr^{-1} respectively. Additionally, declining trends in both observed and simulated AODs in EUS and EUR are significant (at least at p =0.2 level). For the period before 2000, the simulated

AOD in ECH also shows an increasing trend of +0.002 (+1.0%) yr^{-1} which is smaller in magnitude than that after 2000. The opposite trend (though not significant at p=0.2 level) estimated from both AVHRR and TOMS might be explained by limited number of grid values available for calculation (refer to Figure 3). Both simulation and satellite retrievals (except TOMS in EUR which has no trend) show declining trends in EUS and EUR before 2000 with magnitudes comparable to those for the period post-2000, and the declining trend in EUR is significant (at p=0.2 level) in both simulated and AVHRR retrieved AOD.

The model captures the decreasing trends in North Atlantic (NAT) for both the before-2000 and after 2000 periods (as seen in Table 2; Figure 3f). Such declining trends are attributable to decreases in both EUS and EUR. The AOD trends in North Pacific (NPA) before-2000 could possibly be associated with declining trend in global background AOD from biomass burning in southeastern Asia, dust variations in Sahara desert and anthropogenic emission reduction in Japan, Europe and North America. For the period before 2000, both simulated and satellite-retrieved AOD in NPA exhibit declining trends of -0.003 (-2.08%) yr^{-1} and -0.001 to -0.002 (-0.5 to -0.6%) yr^{-1} respectively. However, after 2000, the increase of transport from ECH results in an increasing trend shown in both simulated and most satellite-retrieved AOD (significant at p=0.2 level for SeaWiFS and MISR) in NPA of +0.003 (+2%) yr^{-1} and +0.001 to +0.002 (+0.3 to +1.7%) yr^{-1} respectively, except in AVHRR retrieved AOD which exhibits opposite trend.

The model also captures declining trends in regions influenced mostly by natural mineral dust aerosol, i.e., SHR, CAT and NIN for the period before 2000. Such declining trends might result from a reduction in surface winds over dust source regions in Africa (Ridley et al., 2014). The AOD in CAT also shows a declining trend in most satellite-retrievals for the period after 2000, however the magnitude, i.e., up to -0.006(-1.6%) yr^{-1} is much smaller than that for the

period before 2000 which is up to -0.011(-2.8%) yr^{-1}. Simulations show a similar transition from stronger declining trends of -0.005(-1.9%) yr^{-1} before 2000 to smaller declining trends of 0.000(-0.02%) yr^{-1} after 2000. However, the model fails to capture the increasing trends in the Arabian Desert as well as its downwind ocean area NIN which can be observed from satellite-retrieved AOD (see Figure 2, 3h). Additionally, the simulated increasing trend in SHR has a smaller magnitude of +0.001(+0.33%) than satellite-retrieved AOD trends of +0.002 to +0.15 (+0.5% to +2.3%) except for MODIS-terra. This discrepancy might be caused by the poor representation of dust emissions over the Arabian Desert.

3.1.2 Comparison with AERONET measurement

The spatial location of 693 AERONET sites can be seen in Figure 4a which shows the averaged summer AOD of all available records for each site. The corresponding simulated AOD averaged from the same selected periods which were used to average the observations at each site is given in Figure 4b for comparison. Generally, the spatial gradients of AOD shown in the model is consistent with that from observations. However, the model tends to underestimate AOD both over regions where anthropogenic aerosols are dominant (ECH, EUS and EUR) as well as over regions where natural aerosols are dominant (SHR, CAT and NIN). Such discrepancy is consistent with the comparisons against satellite retrievals in the previous section.

11 AERONET sites which have relatively long-term records were selected for trend analysis and are marked by red boxes in Figure 4a. The simulated AOD as well as the satellite-retrieved AOD is chosen from the corresponding grid cell for each site based on its spatial location. A site by site comparison is presented in Figure 5.

At the Beijing site (Figure 5a) which is in northeastern China, the model agrees with satellite retrievals which show a continual increasing trend from 1990 to 2010. However, the

AOD level from AERONET is much higher than both simulated and satellite-retrieved AOD, and shows an opposite trend. Such discrepancy was also found in our previous analysis when comparing concentrations of precursors against surface observations (Xing et al., 2014). Extremely high AOD levels from AERONET also indicate that the coarse spatial resolution might limit the model's ability to represent the pollution distribution at finer scale. Another site within ECH area is Chen-Kung Univ (Figure 5b) in Taiwan. Simulated and satellite retrieved AOD trends show opposite directions possibly because the model fails to capture variations of biomass burning activities in Southeast Asia as discussed in the previous section. However, the correlation coefficient is relatively high (R=0.44) and the bias is relatively small (NMB=-5%). The AOD measured by AERONET shows a similar increasing trend as the simulation but the correlation is poor.

Simulated, surface-observed and satellite-retrieved AOD are found to be consistent with each other in the other two land areas where anthropogenic aerosols are dominant, i.e., EUS and EUR. At the GSFC site (Figure 5c) in EUS, all AODs show declining trends of -0.007 to -0.013 yr^{-1} which is slightly higher than that of the region averaged trend of -0.003 to -0.008 yr^{-1}. The correlation coefficient between the simulated and observed AOD ranges between 0.42 and 0.57, but the underestimation is >40% due to the underestimation of fine particles (Xing et al., 2014). At the Lille site (Figure 5d) in EUR, simulated, surface-observed and satellite-retrieved AODs show consistent decreasing trends of -0.003 to -0.007 yr^{-1} which are comparable with the region averaged level. The correlation between the simulated and observed AOD ranges between 0.17 and 0.19 and the smaller NMB of <±15% compared to the EUS region likely is attributable to a better simulation of fine particle concentrations (Xing et al., 2014).

At the HJAndrews site (Figure 5e) on the western coast of the U.S. where fewer emission

reductions occurred than in the EUS, the simulated AOD shows a slightly increasing trend of +0.001 yr^{-1} which is also found in surface-observed and satellite-retrieved AOD. Such increasing trends might be associated with the increased AOD level in NPA after 2000. At Bonanza Creek (Figure 5f), the model fails to capture the abnormal high AOD level observed by both AERONET and satellites for the years of 2004 and 2009, when large forest fires occurred in Alaska (National Interagency Fire Center, http://www.nifc.gov/fireInfo/fireInfo_stats_lgFires.html) resulting in significantly enhanced PM burden. At Mauna Loa (Figure 5g) located in Hawaiian Islands, the model overestimates the AOD level compared to both AERONET and satellites observations, resulting from the uncertainties of wind-blown dust emissions. The AERONET monitored AOD is even lower than the satellite retrievals, which might be explained by the high elevation (3400m) of this AERONET site.

However, the model tends to underestimate AOD by 30-60% in areas where mineral dust aerosols are dominant. At the Banizoumbou site (Figure 5h) in Sahel, south of the Sahara Desert, increasing trends of +0.004 to +0.017 yr^{-1} shown in both surface-observed and satellite-retrieved AOD are successfully captured by the model which shows a similar increasing trend of +0.010 yr^{-1}. Also the correlation between the simulated and observed AOD is fairly good ($R>0.5$). At the Cape Verde site (Figure 5i) in CAT where most satellites show continual decreasing trends, AOD observed by AERONET shows a slight increasing trend of +0.005 yr^{-1}. A similar increasing trend is also evident in the simulated AOD, i.e., +0.002 yr^{-1}. Another site where the model agrees with AERONET better than satellites is Sede Boker (Figure 5j) in Israel, between the Sahara Desert and the Arabian Desert. The small declining trend of AOD observed by AERONET is captured by the model, with better correlation and smaller bias than compared with satellite-retrieved

AOD. However, at Solar Village (Figure 5k) in the Arabian Desert, the model fails to capture increasing trends of AOD observed in both AERONET and satellites which is consistent with the finding we discussed in the previous section.

3.2 Trends in clear-sky SWR

3.2.1 Comparison with CERES

The upwelling clear-sky SWR at TOA represents the solar radiation reflected back to space by surface albedo as well as atmospheric aerosols. If surface albedo changes are negligible, its variation is indicative of the changes in top of the atmosphere cooling effects due to aerosols. The spatial distributions of observed and simulated clear-sky SWR at TOA are presented in Figure 6 for 2000 and 2010. Higher values are shown in the areas with highly reflective surface, i.e., ice covered and desert land areas where ground-surface albedo is higher. Because the aerosol radiative effect has been considered in the feedback case, the simulated TOA SWR is higher than that in non-feedback case particularly in regions with high AOD levels such as ECH and SHR, and also compares better with the CERES data relative to the simulation without aerosol feedback effects. However, simulated clear-sky TOA SWRs over desert areas, EUS, EUR and south Asia are still lower than those derived by CERES due to the underestimation of natural and anthropogenic aerosols.

The spatial distribution of land-use types in the model is kept unchanged for the 21-year period. Therefore, there is no clear trend of SWR in the non-feedback case over the entire domain except over the Artic Ocean where simulated ice cover is melting leading to a significant declining trend of TOA SWR. This is also evident in the CERES data. The TOA SWR trend in the feedback case which also represents the trend of DRE shows a similar spatial pattern as the AOD trend shown in Figure 2. A comparison of the time-series of the TOA SWR anomaly

(anomaly to the average of 2000-2010, as seen in Figure 7) also suggests better agreement with observations for the feedback simulation in which the correlation with observations is higher than that in the no-feedback case.

For the period of 2000-2010, the simulated TOA SWR from the feedback case exhibits a significant increasing trend of +0.301 W m^{-2} (+42%) yr^{-1} in ECH, a decreasing trend of -0.095 W m^{-2} (-0.14%) yr^{-1} in EUS and a decreasing trend of -0.106 W m^{-2} (-0.15%) yr^{-1} in EUR (as seen in Figure 7a-c; Table 3). Similar trends are evident in the CERES-derived TOA SWR which shows a relatively smaller increasing trend of +0.103 W m^{-2} (+14%) in ECH, but fairly comparable decreasing trends of -0.099 W m^{-2} (-0.14%) and -0.116 W m^{-2} (-0.17%) yr^{-1} in EUS and EUR respectively. No observed satellite-derived TOA SWR is available back to 1990s, however, the sign of the simulated TOA SWR trends agree well with corresponding sign of the simulated and observed AOD trends in each region (Table 3).

The simulated TOA SWR in NPA (Figure 7e) shows a declining trend of -0.092 W m^{-2} (-0.17%) yr^{-1} before 2000 and an increasing trend of +0.107 W m^{-2} (+0.20%) yr^{-1} after 2000, which are consistent with the AOD trends for each period. The increasing trend in TOA SWR after 2000 is noticeable in CERES data as well, with a relatively smaller increasing trend of +0.057 W m^{-2} (+0.13%) yr^{-1}. In NAT (Figure 7f), the simulated TOA SWR is decreasing for the whole period, with a stronger declining trend of -0.136 W m^{-2} (-0.25%) yr^{-1} from 1990 to 2000 compared to the trend of -0.039 W m^{-2} (-0.07%) yr^{-1} for the period after 2000. The decrease in TOA SWR in this region is associated with the corresponding reduction in AOD which also shows more significant decreasing for the period before 2000. However, the declining trend from the model for 2000-2010 is too weak to be observed in CERES data which shows a small increasing trend of +0.023 W m^{-2} (+0.05%) yr^{-1}.

The decreasing AOD in the Sahara Desert leads to a decreasing TOA SWR trend in the downwind ocean region CAT which is noticeable in both simulation and CERES data. More evidence of a decreasing trend in TOA SWR is shown in the simulation for the period before-2000 than that for the period after-2000 because the reduction of AOD in CAT is greater before-2000 than after. The model also captured the increasing TOA SWR trend in Sahel which is also evident in CERES.

The significant declining trend in SHR for the period of 1990-2000 simulated by the model is associated with the corresponding decreases in AOD. However, the model fails to capture the slightly increasing trend observed by CERES over the Arabian Desert (as seen in Figure 6a), also resulting in a failure to capture the increasing trend in NIN for the period of 2000-2010 (Figure 6a, 7h). This discrepancy is consistent with those noted in the AOD comparison, i.e., that simulated AOD in NIN shows a decreasing trend but observed AOD is increasing.

Higher surface SWR is shown in the mid-latitude regions where the solar zenith angle is high during Jun-Aug. The surface SWR is also influenced by the water vapor in the atmosphere, therefore the desert areas (and downwind ocean regions) with relative dry air show higher surface SWR compared to other areas located at the same latitude (see Figure 6b). Due to aerosol direct radiative effects, the simulated surface SWR decreases in the feedback case compared to the no-feedback case and is more comparable to the surface SWR derived from CERES. The surface SWR in ECH and EUS shows a noticeable reduction from the no-feedback to the feedback case but is still overestimated compared to that derived by CERES. A more pronounced reduction in surface SWR caused by aerosol direct radiative effects is shown in regions dominated by natural dust aerosols, because the reduction of surface SWR in dust areas (and downwind ocean regions) is also caused by the decrease of near-ground albedo due to decreases

of wind-blown dust emissions stemming from the lower wind-speed which is one of the climate responses to the aerosol radiative effects.

For the period of 2000-2010, the surface SWR simulated in the feedback case exhibits a declining trend of -0.56 W m^{-2} (-0.17%) yr^{-1} in ECH (Figure 7a), and an increasing trend of +0.097 W m^{-2} (+0.03%) yr^{-1} and +0.141 W m^{-2} (+0.04%) yr^{-1} in EUS (Figure 7b) and EUR (Figure 7c) respectively, with fairly good agreement with those derived from CERES (R>0.5, which is much better than that calculated from the no-feedback case). Note that the simulated surface SWR trends in both EUS and EUR are considerably lower than CERES.

Similar to TOA SWR, the surface SWR trend in NPA also shows opposite directions for the periods before and after 2000 (Figure 7e); an increasing surface SWR trend of +0.129 W m^{-2} (+0.04%) yr^{-1} before 2000 but decreasing by -0.106 W m^{-2} (-0.03%) yr^{-1} after 2000. Good agreement (R=0.45) is found with CERES-derived surface SWR which also exhibits a significantly declining trend of -0.334 W m^{-2} (-0.10%) $yr^{-1}$from 2000-2010. The simulated increasing trend in NAT (Figure 7f) is stronger before 2000 than for the period after 2000, whereas CERES-derived surface SWR shows a small trend in the opposite direction which is consistent with the discrepancy found in TOA SWR.

The model fails to capture the increasing trend in surface SWR shown in most parts of SHR (Figure 6b). However, the simulation has a good agreement with that derived from CERES (R=0.49) from the series comparison of surface SWR anomaly, suggesting that the variation of dust is too large to present a clear trend within a relative short time period. Such discrepancy might contribute to the bias in reproducing surface SWR in the downwind CAT region where the simulated and observed surface SWR trends present opposite directions for the period of 2000-2010. However, for the period of 1990-2000 when the reduction of dust aerosol in SHR is

significant, the surface SWR in both SHR and CAT as expected present increasing trends. In NIN (Figure 7h), the decreasing trend from 2000-2010 shown in CERES-derived surface SWR is associated with the increase of dust aerosol from Arabian Desert where the model fails to reproduce the observed AOD trend. The simulated surface SWR has a good correlation (R=0.57) with CERES data, though shows a slight trend in the opposite direction. The increasing trend of surface SWR as well as the decreasing trend of TOA SWR in NIN for the period of 1990-2010 is associated with the decreasing trend of AOD for the same period.

3.2.2 Comparison with SURFRAD

To further investigate the model's ability in reproducing the historical clear-sky SWR at the surface, we compared results from simulations of feedback and no-feedback cases with observations at SURFRAD sites. The simulation data is selected from grid cells corresponding to the spatial locations of each SURFRAD site at the time of the measurement, and then grouped to a regional level, i.e., the eastern and western US. The CERES data is also selected for each corresponding site for comparison, but not necessarily for the same time periods since CERES data are monthly mean including all hours.

In general, the simulated clear-sky surface SWR agrees better with SURFRAD than with CERES, with higher correlation coefficients (Figure 8). The increasing trend in the eastern US simulated by the model in the feedback case of +0.31 W m^{-2} yr^{-1} is more comparable with that observed by SURFRAD (+0.52 W m^{-2} yr^{-1}) than CERES (+1.37 W m^{-2} yr^{-1}) even though the CERES data is monthly mean of 24 hours which is lower than daytime averages from both SURFRAD and the simulations. However, the model fails to reproduce some of the yearly variations (e.g., the sharp decrease during 1998-2000) which are evident in SURFRAD, suggesting the need for simulations conducted on a finer spatial scale with more accurate

spatially resolved emissions.

The clear increasing trend of +0.62 W m^{-2} yr^{-1} shown in SURFRAD in the western US is associated with the increasing clear-sky diffuse radiation which might be influenced by factors other than aerosols (e.g., air traffic activities) (Gan et al., 2014). The model shows no trends because most reductions in aerosols occurred in EUS. CERES even shows a declining trend of -0.93 W m^{-2} yr^{-1} in the western US. The discrepancy in the two observation-derived trends suggests that there is a need to further improve the accuracy of observed surface SWR data as well.

3.3 Aerosol direct radiative effect (DRE)

We estimated the DRE as the difference in clear-sky SWR with and without aerosols. It is easy to estimate the DRE from the model simulations by taking the difference of clear-sky SWR between the feedback case and no feedback case. The simulated DRE at both TOA and surface is shown in Table 4 and Figure 9. Also, we compared the modeled results with the values of measurement-based assessments summarized in Yu et al. (2006). All the values of "measured" DREs mentioned in subsequent discussions are obtained from Yu et al. (2006). Since it is impossible to remove all aerosols from the real atmosphere, the DRE cannot be directly observed. The measurement-based method needs the adoption of radiative transfer model or other assumptions to estimate DRE. For example, Remer and Kaufman (2006) put the results of the MODIS aerosol retrieval as an internally consistent set of aerosol optical properties into a column radiative transfer climate model (i.e., CLIRAD-SW) to calculate the upwelling hemispheric broadband fluxes and the aerosol effects at TOA. Zhang et al. (2005a, b) calculated the shortwave aerosol radiative forcing over the global oceans by using the 20 km resolution CERES measurements as well as the aerosol dependent angular distribution models.

The TOA-DRE is evident (|DRE|> 4 W m^{-2}) in all 8 regions except SHR where the surface-reflected upwelling radiation can be reduced by the aerosol absorption leading to a significant reduction of TOA-DRE (Kim et al., 2005). From the 1990s to the 2000s on a decadal average basis, the simulated TOA-DRE in ECH increased by 30% due to the increased aerosol burden. A more significant increasing trend is shown in the 2000s compared to 1990s. The simulated TOA-DRE in ECH shows comparable values with the measured one over the land of eastern Asia (Yu et al., 2006). The reduction of aerosols in EUS / EUR mitigated the TOA-DRE by 19% / 20% from 1990s to 2000s. The simulated TOA-DRE agrees with the measured one in EUR, but has lower values in EUS. Also the simulated TOA-DRE in SHR is significantly lower than measurements. The underestimation of TOA-DRE in EUS and SHR might be associated with the underestimation of the aerosol burden (as indicated by the comparison of simulated and observed AOD). In NPA, the TOA-DRE shows similar opposite trends (before and after 2000) which is consistent with the trends of AOD and clear-sky TOA SWR, and is slightly lower than measurements, but comparable with those simulated by GCMs as -3.6 to -11.7 W m^{-2} (Yu et al, 2006). The decrease of AOD level in NAT also reduced the TOA-DRE by 9%, with more significant trend in the 1990s. The simulated TOA-DRE is within the measured range. Continual decrease of AOD in CAT slightly decreased the TOA-DRE by 2% from 1990s to 2000s. The magnitude of simulated TOA-DRE agrees well with the measured one. Though the model fails to capture the increasing trend of AOD observed at NIN, the simulated TOA-DRE agrees with measurements.

The surface-DRE shows a similar spatial distribution as TOA-DRE except that a stronger DRE is shown in SHR. Trends in surface-DRE at each site are consistent with those in TOA-DRE which have the same direction during the corresponding periods. Over land regions the

simulated surface-DRE is about 2 times as much as the TOA-DRE for ECH, EUS and EUR, and about 6 times for SHR. On a global scale, the surface-DRE (-13.5 to -17.4W m^{-2}) derived by the satellite-model integrated approaches (Yu et al. 2006) is about 3.4 times as large as the TOA-DRE (-5.3 to -6.6 W m^{-2}). The surface-DRE (-14.4 to -30.4 W m^{-2}) derived by AERONET is about 2.2-3.8 times as large as the derived TOA-DRE (-5.2 to -11.1 W m^{-2}) (Yu et al. 2006). Like many GCMs, the simulated surface-DRE over land is very likely to be underestimated in this study, because the simulated TOA-DRE by the model is comparable (in ECH, EUR) or lower (in EUS, SHR) than measurement-derived values but the ratio of surface-DRE / TOA-DRE estimates in this study is lower than measurement-derived values.

Over ocean regions, the simulated surface-DRE (-7.3 to -18.9 W m^{-2}) is about 1.4-1.8 times as much as the TOA-DRE (-5.1 to -11.1 W m^{-2}). The ratio is comparable with that found from measurements-based estimates which show the global ocean averaged surface-DRE (-9.3 to -11.9 W m^{-2}) about 1.6 times as much as the measured TOA-DRE (-3.5 to -7.0 W m^{-2}) (Yu et al., 2006).

4. Discussion

Successful estimates of DRE trends depend on accurate estimates of AOD as well as the aerosol direct radiative efficiency (E_τ) which is defined as the DRE per unit aerosol optical depth and has been used for comparisons among different methods (Yu et al., 2006). The E_τ in this study can be estimated simply by using DRE divided by AOD. The relationship between DRE and AOD is close to linear under low AOD conditions (Chung et al., 2012). Thus, the slope of the linear regression between ΔSWR and ΔAOD can provide a close estimate of E_τ, denoted as E_τ^* (e.g., Satheesh and Ramanathan, 2000).

However, the E_τ^* (estimated as the slope of the linear regression between DRE and AOD) is smaller in magnitude (i.e., absolute value) than E_τ at high AOD levels. This is illustrated in

Figure 10 which displays the relationship between average daytime clear-sky DRE and AOD (note that each point in these figures represents a daily average value). It is noticeable that the response of DRE to AOD becomes non-linear at high AOD, more apparent in the relationships for SHR region where the AOD is higher. Consequently, in this regime of high AOD the estimated $E_\tau^* < E_\tau$. Additionally, Yu et al (2006) noted smaller radiative efficiencies for anthropogenic aerosols with higher absorbing components. This may also result in $E_\tau^* < E_\tau$ in regions of anthropogenic aerosols (such as ECH, EUS and EUR).

To further explore the response of clear-sky SWR to the AOD level, we further analyzed data over an 11-year period (2000-2010). To minimize the influence of month to month variability (e.g., associated with solar zenith angle) among June, July and August, monthly-averaged SWR and AOD were deseasonalized by subtracting the average of 11-year data for the corresponding month (see Figure S1). We chose 24hour-averaged SWR but AOD at noon (local-time) to be consistent with the observation-derived data from CERES-EBAF and satellite-retrievals. The estimated radiative efficiency based on 24 hour average SWR to noon AOD (noted as $E_{\tau 2}^*$) is about half of the value of E_τ.

Table 5 presents the estimates of E_τ, E_τ^* and observed and simulated $E_{\tau 2}^*$ at both TOA and surface for 8 regions. The measurement-based E_τ summarized in Yu et al. (2006) (noted as $E_{\tau\text{-yu}}$) is used to compare the estimates in this study.

Over land regions where anthropogenic aerosols are dominant, the simulated E_τ at TOA in ECH, EUS and EUR is about -45.4, -49.6 and -57.2 W m^{-2} τ^{-1} respectively, which are slightly larger in magnitude than the measurement-derived TOA-E_τ which is about -9 to -33, -24 to -37 and -11 to -34 W m^{-2} τ^{-1}, respectively. Furthermore, the simulated TOA-$E_{\tau 2}^*$ is also much higher than those derived from observations. One possible reason for this discrepancy is the moderate

underestimation of AOD since in most cases TOA-E_τ is larger when AOD is low. Such overestimation of TOA-E_τ may compensate for the underestimation of AOD resulting in a comparable TOA-DRE in these regions.

The simulated E_τ at the surface is about -90.8, -101.5 and -114.3 W m^{-2} τ^{-1} for ECH, EUS and EUR respectively which is higher than measurement-derived surface-E_τ of -51 to -106, -65 to -84 and -57 to -98 W m^{-2} τ^{-1}. However, surface-E_τ^* has much lower values than surface-E_τ, thus it is comparable with measurement-derived surface-E_τ. The simulated surface-$E_{\tau 2}^*$ also shows good agreement with observed estimates (-40 to -60 $Wm^{-2}\tau^{-1}$). Discrepancies are found in the EUS where simulated surface-$E_{\tau 2}^*$ is the lowest but observed surface-$E_{\tau 2}^*$ is highest of all regions. Lower surface-$E_{\tau 2}^*$ in US in the feedback case might be associated with the unexpected positive correlation (with slope = +14.97 Wm^{-2} τ^{-1}) between surface SWR and AOD in the non-feedback case (See Table 5). With the agreement in surface-E_τ, the underestimation of surface-DRE in EUS, EUS and EUR is primarily associated with the underestimation of AOD level.

The feedback from reduction in TOA-DRE by aerosol absorption results in a relative lower TOA-$E_{\tau 2}^*$ over SHR than those in other regions for both observation and simulation. However, the simulated TOA- $E_{\tau 2}^*$ is twice as much as observed, suggesting overestimation of TOA- E_τ in SHR as well.

Over the ocean regions, both simulated E_τ and E_τ^* at TOA in NPA (-66.9 and -60.9 Wm^{-2} τ^{-1}) and NAT (-65.3 and -59.2 Wm^{-2} τ^{-1}) are higher than those measurement-derived TOA-E_τ which are about -31 to -52 and -32 to -41 Wm^{-2} τ^{-1} respectively. Also the simulated TOA-$E_{\tau 2}^*$ is also higher than that derived from observations. The overestimation (by 60-70%) of TOA- $E_{\tau 2}^*$ in NPA and NAT is not as significant as that in land regions (110-190%), therefore the simulated TOA-DRE over NPA and NAT is still within the range of measurement-based estimates. The

simulated surface- E_τ and E_τ^* for NPA (-96.9 and -68.8 Wm^{-2} τ^{-1}) and NAT (-98.7 and -59.2 Wm^{-2} τ^{-1}) are consistent with those measurement-derived values which are -61 to -90 and -60 to -90 W m^{-2} τ^{-1}. Also the simulated surface-$E_{\tau 2}^*$ agrees with the observation derived values. Therefore the model successfully reproduces the observed surface-DRE over NAP and NAT.

In the other two ocean regions where natural dust is dominant (i.e., CAT and NIN), the simulated TOA- E_τ and E_τ^* are overestimated compared to measurement-derived data. The simulated TOA- $E_{\tau 2}^*$ is also higher than that derived from observations. The surface- E_τ and E_τ^* tend to be overestimated as well in these regions, the observed surface-$E_{\tau 2}^*$ is much lower than that in other regions, whereas the simulated surface-$E_{\tau 2}^*$ in these regions are comparable with others. A possible reason is that surface SWR shows a nonlinear response with AOD (showing smaller slope, i.e., E_τ) when AOD levels are high. The model fails to capture the extremely high AOD observed by satellites, and consequently overestimates the $E_{\tau 2}^*$ in these regions. Such overestimation of both TOA- and surface- E_τ may compensate for the underestimation of AOD resulting in a comparable TOA- and surface- DRE in these regions.

5. Conclusion

A 21 year simulation from 1990-2010 over the northern hemisphere was conducted with a coupled meteorology-chemistry model. In general, the model captured historical AOD trends of 21 years in most regions, including the continual increasing trend in ECH; decreasing trend for EUS, EUR and NAT, and the decreasing in 1990s but increasing trend in 2000s in SHR and NPA. The model also captured the decreasing trend in NIN before 2000, but failed to capture its increasing trend after 2000. That discrepancy as well as the underestimation of AOD over regions which have substantial natural dust aerosol contributions might be associated with the uncertainty in estimation of wind-blown dust in the model. Slight underestimations in ECH and

EUS might be associated with underestimation of fine particles as well as the poor representation of secondary organic aerosol formation which is more evident in summer. The simulation with aerosol radiative effects successfully captured the historical clear-sky SWR at both TOA and surface in ECH, EUS and EUR. The model also captured the enhanced DRE in NPA at both TOA and surface after 2000s. However, discrepancies are found over dust regions due to the uncertainties from AOD estimations in these regions.

The DRE estimation requires not only accurate estimates of AOD, but also of correct aerosol radiative efficiency. Unfortunately, neither has a certain value from measurement-based studies which still present a wide range of values (Yu et al., 2006; Chin et al., 2014). Uncertainties therefore limit the accuracy of DRE estimation. The same issue applies to the model as well. Estimates of TOA-DRE are comparable with those derived from measurements for most regions; however, overestimates of TOA-E_τ may be compensating for the underestimations of AOD. Such overestimates of TOA-E_τ might be associated with the uncertainties of the ratio of scatting aerosols to total aerosols (e.g., a larger TOA-E_τ is expected when the change in absorption aerosols is larger than scattering aerosols). Compared to previous estimates from GCMs, the simulated surface- E_τ in this study agrees better with those derived by the measurements. However, surface-DRE trends are underestimated due to underestimated AOD in land regions. Further improvement of simulated TOA-E_τ as well as both anthropogenic and natural AOD is important. An accurate temporally resolved biomass emission inventory (van der Werf et al., 2006; Shi and Yamaguchi, 2014), an improved dust emission model (Kok et al, 2014) and an advance scheme to model atmospheric organic aerosol (Koo et al., 2014; Zhao et al., 2015) are suggested for future model investigations. We are currently conducting a similar study with a finer-scale simulation and relatively better spatially and temporally resolved

emission inventories over the continental U.S. domain. Further analysis of those model calculations and assessment of the impacts of the higher resolution emissions can be found in Gan et al. (2015).

Acknowledgements

Although this work has been reviewed and approved for publication by the U.S. Environmental Protection Agency (EPA), it does not reflect the views and policies of the agency. This work was supported in part by an inter-agency agreement between the Department of energy project (IA number is DE-SC000378) and EPA (IA number is RW-89-9233260 1). This research was performed while Jia Xing and Chuen-Meei Gan held a National Research Council Research Associateship Award at US EPA. The authors gratefully acknowledge the availability of AVHRR, TOMS, SeaWiFS, MISR, MODIS-terra and –aqua, CERES, AERONET, SURFRAD data.

References

Albrecht, B. A.: Aerosols, cloud microphysics, and fractional cloudiness, Science, 245, 1227–1230, 1989.

Anantharaj, V. G., Nair, U. S., Lawrence, P., Chase, T. N., Christopher, S., and Jones, T.: Comparison of satellite‐derived TOA shortwave clear‐sky fluxes to estimates from GCM simulations constrained by satellite observations of land surface characteristics. International Journal of Climatology, 30(13), 2088-2104, 2010.

Bohren, CF, and DR Huffman.: Absorption and Scattering of Light by Small Particles. Wiley-

Interscience, New York, P530, 1983

Chan, P. K., Zhao, X., and Heidinger, A. K.: Long-term aerosol climate data record derived from operational AVHRR satellite observations, Dataset Papers in Geosciences, available at: http://www.hindawi.com/journals/dpis/2013/140791/ (last access: 12 May 2015), 2013, 140791, doi:10.7167/2013/140791, 2013.

Chin, M., Diehl, T., Tan, Q., Prospero, J. M., Kahn, R. A., Remer, L. A., Yu, H., Sayer, A. M., Bian, H., Geogdzhayev, I. V., Holben, B. N., Howell, S. G., Huebert, B. J., Hsu, N. C., Kim, D., Kucsera, T. L., Levy, R. C., Mishchenko, M. I., Pan, X., Quinn, P. K., Schuster, G. L., Streets, D. G., Strode, S. A., Torres, O., and Zhao, X.-P.: Multi-decadal aerosol variations from 1980 to 2009: a perspective from observations and a global model, Atmos. Chem. Phys., 14, 3657-3690, doi:10.5194/acp-14-3657-2014, 2014.

Chu, D. A., Kaufman, Y. J., Ichoku, C., Remer, L. A., Tame, D., and Holben, B. N.: Validation of MODIS aerosol optical depth retrieval over land, Geophys. Res. Lett., 29, 1617–1621, 2002.

Chung, C. E.: Aerosol direct radiative forcing: a review, in: Atmospheric Aerosols– Regional Characteristics – Chemistry and Physics, edited by: Abdul-Razzak, H., ISBN: 978-953-51-0728-6, InTech, available at: http://www.intechopen.com/books/atmospheric-aerosols-regional-characteristics-chemistry-and-physics/aerosol-direct-radiative-forcing-a-review (last access: 12 May 2015), 2012.

Clough, S. A., Shephard, M. W., Mlawer, E. J., Delamere, J. S., Iacono, M. J., Cady-Pereira, K., Boukabara, S., and Brown, P. D., Atmospheric radiative transfer modeling: a summary of the AER codes, J. Quant. Spectrosc. Ra., 91, 233–244, 2005.

Deng, X., Tie, X., Zhou, X., Wu, D., Zhong, L., Tan, H., Li, F., Huang, X., Bi, X. and Deng, T.:

Effects of Southeast Asia biomass burning on aerosols and ozone concentrations over the Pearl River Delta (PRD) region. Atmospheric Environment, 42(36), 8493-8501, 2008

Freidenreich, S. M., and Ramaswamy, V.: Analysis of the biases in the downward shortwave surface flux in the GFDL CM2.1 general circulation model, J. Geophys. Res., 116, D08208, doi:10.1029/2010JD014930, 2011.

Fu, J. S., Hsu, N. C., Gao, Y., Huang, K., Li, C., Lin, N.-H., and Tsay, S.-C.: Evaluating the influences of biomass burning during 2006 BASE-ASIA: a regional chemical transport modeling, Atmos. Chem. Phys., 12, 3837-3855, doi:10.5194/acp-12-3837-2012, 2012.

Fu, X., Wang, S. X., Cheng, Z., Xing, J., Zhao, B., Wang, J. D., and Hao, J. M.: Source, transport and impacts of a heavy dust event in the Yangtze River Delta, China, in 2011, Atmos. Chem. Phys., 14, 1239-1254, doi:10.5194/acp-14-1239-2014, 2014.

Gan, C.-M., Pleim, J., Mathur, R., Hogrefe, C., Long, C. N., Xing, J., Roselle, S., and Wei, C.: Assessment of the effect of air pollution controls on trends in shortwave radiation over the United States from 1995 through 2010 from multiple observation networks, Atmos. Chem. Phys., 14, 1701–1715, 2014.

Gan, C.-M., Pleim, J., Mathur, R., Hogrefe, C., Long, C. N., Xing, J., Wong, D., Gilliam, R., and Wei, C.: Assessment of multi-decadal WRF-CMAQ simulations for understanding direct aerosol effects on radiation "brightening" in the United States, Atmos. Chem. Phys. Discuss., 15, 17711-17742, doi:10.5194/acpd-15-17711-2015, 2015.

Hakuba, M. Z., Folini, D., Schaepman‐Strub, G. and Wild, M.: Solar absorption over Europe from collocated surface and satellite observations. Journal of Geophysical Research: Atmospheres, 119(6), 3420-3437, 2014

Hogrefe, C., Pouliot, G., Wong, D., Torian, A., Roselle, S., Pleim, J., and Mathur, R.: Annual

application and evaluation of the online coupled WRF–CMAQ system over North America under AQMEII phase 2. Atmospheric Environment, 115, 683-694, 2015.

Holben, B. N., Tanre, D., Smirnov, A., Eck, T. F., Slutsker, I., Abuhassan, N., Newcomb, J., Schafer, W. W., Chatenet, B., Lavenue, F., Kaufman, Y. J., Vande Castle, J., Setzer, A., Markham, B., Clark, D., Frouin, R., Halthore, R., Karnieli, A., O'Neill, N. T., Pietras, C., Pinker, R. T., Voss, K., and Zibordi, G.: An emerging ground-based aerosol climatology: Aerosol optical depth from AERONET, J. Geophys. Res., 106, 12067–12097, 2001.

Hsu, N. C., Gautam, R., Sayer, A. M., Bettenhausen, C., Li, C., Jeong, M. J., Tsay, S.-C., and Holben, B. N.: Global and regional trends of aerosol optical depth over land and ocean using SeaWiFS measurements from 1997 to 2010, Atmos. Chem. Phys., 12, 8037-8053, doi:10.5194/acp-12-8037-2012, 2012.

Hsu, N. C., Tsay, S.-C., King, M. D., and Herman, J. R.: Aerosol properties over bright-reflecting source regions, IEEE T. Geosci. Remote, 42, 557–569, 2004.

Intergovernmental Panel on Climate Change (IPCC): Chapter 8-Anthropogenic and Natural Radiative Forcing, Climate change 2013: The Physical Science Basis, Cambridge Univ. Press, New York, Cambridge University Press, 659-740, 2014

Kahn, R. A., Gaitley, B. J., Garay, M. J., Diner, D. J., Eck, T., Smirnov, A., and Holben, B. N.: Multiangle Imaging SpectroRadiometer global aerosol product assessment by comparison with the Aerosol Robotic Network, J. Geophys. Res., 115, D23209, doi:10.1029/2010JD014601, 2010.

Kahn, R., Gaitley, B., Martonchik, J., Diner, D., Crean, K., and Holben, B.: MISR global aerosol optical depth validation based on two years of coincident AERONET observations, J. Geophys. Res., 110, D10S04, 2005, doi:10.1029/2004JD004706

Kato, Seiji, Norman G. Loeb, Fred G. Rose, David R. Doelling, David A. Rutan, Thomas E. Caldwell, Lisan Yu, Robert A. Weller: Surface Irradiances Consistent with CERES-Derived Top-of-Atmosphere Shortwave and Longwave Irradiances. J. Climate, 26, 2719–2740. 2013, doi: http://dx.doi.org/10.1175/JCLI-D-12-00436.1

Kaufman, Y. J., Tanré, D., Remer, L., Vermote, E., Chu, A., and Holben, B. N.: Operational remote sensing of tropospheric aerosol over land from EOS moderate resolution imaging spectroradiometer, J. Geophys. Res., 102, 17051–17067, 1997.

Kim, D., Sohn, B. J., Nakajima, T., and Takemura, T.: Aerosol radiative forcing over east Asia determined from ground-based solar radiation measurements, J. Geophys. Res., 110, D10S22, doi:10.1029/2004JD004678, 2005.

Kok, J. F., Mahowald, N. M., Fratini, G., Gillies, J. A., Ishizuka, M., Leys, J. F., Mikami, M., Park, M.-S., Park, S.-U., Van Pelt, R. S., and Zobeck, T. M.: An improved dust emission model – Part 1: Model description and comparison against measurements, Atmos. Chem. Phys., 14, 13023-13041, doi:10.5194/acp-14-13023-2014, 2014.

Koo, B., Knipping, E., and Yarwood, G.: 1.5-Dimensional volatility basis set approach for modeling organic aerosol in CAMx and CMAQ. Atmospheric Environment, 95, 158-164, 2014.

Levy, R. C., Remer, L. A., Kleidman, R. G., Mattoo, S., Ichoku, C., Kahn, R., and Eck, T. F.: Global evaluation of the Collection 5 MODIS dark-target aerosol products over land, Atmos. Chem. Phys., 10, 10399–10420, doi:10.5194/acp-10-10399-2010, 2010.

Lin, J., Nielsen, C. P., Zhao, Y., Lei, Y., Liu, Y., and McElroy, M. B.: Recent changes in particulate air pollution over China observed from space and the ground: effectiveness of emission control. Environmental science & technology, 44(20), 7771-7776, 2010.

Liu, X. H., Zhang, Y., Cheng, S. H., Xing, J., Zhang, Q., Streets, D. G., Jang, C., Wang, W. X., and Hao, J. M.: Understanding of regional air pollution over China using CMAQ, part I performance evaluation and seasonal variation. Atmospheric Environment, 44(20), 2415-2426, 2010

Loeb, N. G., Wielicki, B. A., Doelling, D. R., Smith, G. L., Keyes, D. F., Kato, S., Manalo-Smith, N., and Wong, T.: Toward optimal closure of the earth's top-of-atmosphere radiation budget. Journal of Climate, 22, 748–766, doi: 10.1175/2008JCLI2637.1, 2009

Loeb, N. G., Lyman, J. M., Johnson, G. C., Allan, R. P., Doelling, D. R., Wong, T., Soden, B.J. and Stephens, G. L.: Observed changes in top-of-the-atmosphere radiation and upper-ocean heating consistent within uncertainty. Nature Geoscience, 5, 110-113, 2012

Long, C. N. and Ackerman, T. P.: Identification of clear skies from broadband pyranometer measurements and calculation of downwelling shortwave cloud effects, J. Geophys. Res., 105, 15609–15626, doi:10.1029/2000JD900077, 2000.

Marsham, J. H., Knippertz, P., Dixon, N. S., Parker, D. J., and Lister, G. M. S.: The importance of the representation of deep convection for modeled dust-generating winds over West Africa during summer, Geophys. Res. Lett., 38, L16803, doi:10.1029/2011GL048368, 2011.

Mathur, R., Pleim, J., Wong, D., Otte, T. L., Gilliam, R. C., Roselle, S. J.,Young, J. O., Binkowski, F. S., and Xiu, A.: The WRF-CMAQ integrated on-line modeling system: development, testing, and initial applications, in: Air Pollution Modeling and its Applications XX, edited by: Steyn, D. G. and Rao, S. T., Springer, the Netherlands, 155–159, 2010.

Mathur, R., Pleim, J., Wong, D., Hogrefe, C., Xing, J., Wei, C., Gan, C.-M., and Binkowski, F.: Investigation of trends in aerosol direct radiative effects over North America using a

coupled meteorology-chemistry model, in: Air Pollution Modeling and its Application XXIII, Springer International Publishing, Switzerland, 67–72, 2014.

McClain, C. R., Cleave, M. L., Feldman, G. C., Gregg, W. W., Hooker, S. B., and Kuring, N.: Science quality SeaWiFS data for global biospheric research, Sea Technol., 39, 10–16, 1998.

McCormick, R. A. and Ludwig, J. H.: Climate modification by atmospheric aerosols, Science, 156(3780), 1358–1359, 1967.

Mercado, L. M., Bellouin, N., Sitch, S., Boucher, O., Huntingford, C., Wild, M. and Cox P.M.: Impact of changes in diffuse radiation on the global land carbon sink, Nature, 458, 1014–1017, 2009, doi:10.1038/nature07949.

Ohmura, A., and Wild, M.: Is the hydrological cycle accelerating?, Science, 298, 1345–1346, 2002, doi:10.1126/science.1078972.

Ohmura, A., Observed decadal variations in surface solar radiation and their causes, J. Geophys. Res., 114, D00D05, 2009, doi:10.1029/2008JD011290.

Patadia, F., Gupta, P. and Christopher, S. A.: First observational estimates of global clear sky shortwave aerosol direct radiative effect over land, Geophys. Res. Lett., 35, L04810, doi:10.1029/2007GL032314. 2008.

Pleim, J., Young, J., Wong, D., Gilliam, R., Otte, T., and Mathur, R.: Two-way coupled meteorology and air quality modeling, in: Air Pollution Modeling and Its Application XIX, NATO Science for Peace and Security Series C: Environmental Security, 2, edited by: Borrego, C. and Miranda, A. I., Springer, the Netherlands, 496–504, ISBN 978-1-4020-8452-2, 2008.

Prasad, A. K. and Singh, R. P.: Changes in aerosol parameters during major dust storm events

(2001–2005) over the Indo-Gangetic Plains using AERONET and MODIS data, J. Geophys. Res.-Atmos., 112, D09208, doi:10.1029/2006JD007778, 2007.

Rajeev, K., and Ramanathan, V.: Direct observations of clear‐sky aerosol radiative forcing from space during the Indian Ocean Experiment. Journal of Geophysical Research: Atmospheres (1984‐2012), 106(D15), 17221-17235, 2001.

Remer, L. A., Kaufman, Y. J., Tanré, D., Mattoo, S., Chu, D. A., Martins, J. V., Li, R.-R., Ichoku, C., Levy, R. C., Kleidman, R. G., Eck, T. F., Vermote, E., and Holben, B. N.: The MODIS aerosol algorithm, products, and validation, J. Atmos. Sci., 62, 947‐973, 2005.

Remer, L. A. and Kaufman, Y. J.: Aerosol direct radiative effect at the top of the atmosphere over cloud free ocean derived from four years of MODIS data, Atmos. Chem. Phys., 6, 237-253, doi:10.5194/acp-6-237-2006, 2006.

Remer, L. A., Kleidman, R. G., Levy, R. C., Kaufman, Y. J., Tanré, D., Mattoo, S., Martins, J. V., Ichoku, C., Koren, I., Yu, H., and Holben, B. N.: Global aerosol climatology from the MODIS satellite sensors, J. Geophys. Res.-Atmos., 113, D14S07, doi:10.1029/2007JD009661, 2008.

Ridley, D. A., Heald, C. L., and Prospero, J. M.: What controls the recent changes in African mineral dust aerosol across the Atlantic?, Atmos. Chem. Phys., 14, 5735–5747, doi:10.5194/acp-14-5735-2014, 2014.

Roy, B., Mathur, R., Gilliland, A. B., and Howard, S. C.: A comparison of CMAQ-based aerosol properties with IMPROVE, MODIS, and AERONET data, J. Geophys. Res., 112, D14301, 2007, doi:10.1029/2006JD008085

Ruckstuhl, C., and Norris, J., How do aerosol histories affect solar “dimming” and “brightening” over Europe?: IPCC-AR4 models versus observations, J. Geophys. Res., 114, D00D04,

2009, doi:10.1029/2008JD011066.

Satheesh, S. K., and Ramanathan, V.: Large differences in tropical aerosol forcing at the top of the atmosphere and Earth's surface. Nature, 405(6782), 60-63, 2000.

Sayer, A. M., Hsu, N. C., Bettenhausen, C., Jeong, M.-J., Holben, B. N., and Zhang, J.: Global and regional evaluation of over-land spectral aerosol optical depth retrievals from SeaWiFS, Atmos. Meas. Tech., 5, 1761-1778, doi:10.5194/amt-5-1761-2012, 2012.

Shi, Y., and Yamaguchi, Y.: A high-resolution and multi-year emissions inventory for biomass burning in Southeast Asia during 2001–2010. *Atmospheric Environment*, *98*, 8-16, 2014.

Streets, D. G., Wu, Y. and Chin, M., Two-decadal aerosol trends as a likely explanation of the global dimming/brightening transition, Geophys. Res. Lett., 33, L15806, 2006, doi:10.1029/2006GL026471.

Torres O., P.K. Bhartia, J.R. Herman and Z. Ahmad, Derivation of aerosol properties from satellite measurements of backscattered ultraviolet radiation. Theoretical Basis, J. Geophys. Res., 103, 17099-17110, 1998

Torres, O., P.K. Bhartia ,J.R. Herman, A. Sinyuk and B. Holben, A long term record of aerosol optical thickness from TOMS observations and comparison to AERONET measurements, J. Atm. Sci.,59,398-413, 2002

Twomey, S.: The influence of pollution on the shortwave albedo of clouds, J. Atmos. Sci., 34, 1149–1152, 1977.

van der Werf, G. R., Randerson, J. T., Giglio, L., Collatz, G. J., Kasibhatla, P. S., and Arellano Jr., A. F.: Interannual variability in global biomass burning emissions from 1997 to 2004, Atmos. Chem. Phys., 6, 3423-3441, doi:10.5194/acp-6-3423-2006, 2006.

Wang, J., Wang, S., Jiang, J., Ding, A., Zheng, M., Zhao, B., Wong, C.-D., Zhou, W., Zheng, G.,

Wang, L., Pleim, J. and Hao, J.: Impact of aerosol–meteorology interactions on fine particle pollution during China's severe haze episode in January 2013, Environmental Research Letters, 9(9), 094002. doi:10.1088/1748-9326/9/9/094002, 2014.

Wang, L., Jang, C., Zhang, Y., Wang, K., Zhang, Q., Streets, D., Fu, J., Lei, Y., Schreifels, J., He, K., Hao, J., Lam, Y-F., Lin, J., Meskhidze, N., Voorhees, S., Evarts, D., and Phillips, S.: Assessment of air quality benefits from national air pollution control policies in China. Part II: Evaluation of air quality predictions and air quality benefits assessment. Atmospheric Environment, 44(28), 3449-3457, 2010

Wang, S., Xing, J., Chatani, S., Hao, J., Klimont, Z., Cofala, J., & Amann, M.: Verification of anthropogenic emissions of China by satellite and ground observations. Atmospheric Environment, 45(35), 6347-6358, 2011

Wielicki, B. A., Barkstrom, B. R., Baum, B. A., Charlock, T. P., Green, R. N., Kratz, D. P., Lee, R.B., Minnis, P. ; Smith, G.L., Wong, T., Young, D.F., Cess, R.D., Coakley, J.A., Crommelynck, D.A.H., Donner, L., Kandel, R., King, M.D., Miller, A.J., Ramanathan, V., Randall, D.A., Stowe, L.L. and Welch, R. M.: Clouds and the Earth's Radiant Energy System (CERES): algorithm overview. Geoscience and Remote Sensing, IEEE Transactions on, 36(4), 1127-1141, 1998

Wielicki, Bruce A., Bruce R. Barkstrom, Edwin F. Harrison, Robert B. Lee, G. Louis Smith, John E. Cooper: Clouds and the Earth's Radiant Energy System (CERES): An Earth Observing System Experiment. Bull. Amer. Meteor. Soc., 77, 853–868, 1996.

Wild, M., Folini, D., Schär, C., Loeb, N., Dutton, E. G. and König-Langlo, G.: The global energy balance from a surface perspective. Climate dynamics, 40(11-12), 3107-3134, 2013.

Wild, M., Gilgen, H., Roesch, A., Ohmura, A., Long, C. N., Dutton, E. G., Forgan, B., Kallis, A.,

Russak, V., and Tsvetkov, A.: From dimming to brightening: Decadal changes in surface solar radiation, Science, 308, 847–850, 2005, doi:10.1126/science.1103215.

Wild, M., Global dimming and brightening: A review, J. Geophys. Res., 114, D00D16, 2009, doi:10.1029/2008JD011470

Wild, M., Long, C. N., and Ohmura, A.: Evaluation of clear-sky solar fluxes in GCMs participating in AMIP and IPCC – AR4 from a surface perspective, J. Geophys. Res.-Atmos., 111, D01104, doi:10.1029/2005JD006118, 2006.

Wild, M., Ohmura, A., and Makowski, K., Impact of global dimming and brightening on global warming, Geophys. Res. Lett., 34, L04702, 2007, doi:10.1029/2006GL028031.

Wong, D. C., Pleim, J., Mathur, R., Binkowski, F., Otte, T., Gilliam, R., Pouliot, G., Xiu, A., Young, J. O., and Kang, D.: WRF-CMAQ two-way coupled system with aerosol feedback: software development and preliminary results, Geosci. Model Dev., 5, 299-312, doi:10.5194/gmd-5-299-2012, 2012.

Xing, J., Mathur, R., Pleim, J., Hogrefe, C., Gan, C.-M., Wong, D. C., Wei, C., Gilliam, R., and Pouliot, G.: Observations and modeling of air quality trends over 1990–2010 across the Northern Hemisphere: China, the United States and Europe, Atmos. Chem. Phys., 15, 2723-2747, doi:10.5194/acp-15-2723-2015, 2015.

Yu, H., Kaufman, Y. J., Chin, M., Feingold, G., Remer, L. A., Anderson, T. L., Balkanski, Y., Bellouin, N., Boucher, O., Christopher, S., DeCola, P., Kahn, R., Koch, D., Loeb, N., Reddy, M. S., Schulz, M., Takemura, T., and Zhou, M.: A review of measurement-based assessments of the aerosol direct radiative effect and forcing, Atmos. Chem. Phys., 6, 613-666, doi:10.5194/acp-6-613-2006, 2006.

Yu, S., Mathur, R., Pleim, J., Wong, D., Gilliam, R., Alapaty, K., Zhao, C., and Liu, X.: Aerosol

indirect effect on the grid-scale clouds in the two-way coupled WRF–CMAQ: model description, development, evaluation and regional analysis, Atmos. Chem. Phys., 14, 11247–11285, doi:10.5194/acp-14-11247-2014, 2014.

Zhang, J., Christopher, S. A., Remer, L. A., and Kaufman, Y. J.: Shortwave aerosol radiative forcing over cloud-free oceans from Terra. I: Angular models for aerosols, J. Geophys. Res., 110, D10S23, doi:10.1029/2004JD005008, 2005a.

Zhang, J., Christopher, S. A., Remer, L. A., and Kaufman, Y. J.: Shortwave aerosol radiative forcing over cloud-free oceans from Terra. II: Seasonal and global distributions, J. Geophys. Res., 110, D10S24, doi:10.1029/2004JD005009, 2005b.

Zhao, B., Wang, S., Donahue, N. M., Chuang, W., Hildebrandt Ruiz, L., Ng, N. L., Wang, Y., and Hao, J.: Evaluation of One-Dimensional and Two-Dimensional Volatility Basis Sets in Simulating the Aging of Secondary Organic Aerosol with Smog-Chamber Experiments. *Environmental science & technology*, *49*(4), 2245-2254, 2015.

Zhao, X.-P., Chan, P. K., and Heidinger, A. K.: A global survey of the effect of cloud contamination on the aerosol optical thickness and its long-term trend derived from operational AVHRR satellite observations, J. Geophys. Res., 118, 2849–2857, doi:10.1002/jgrd.50278, 2013.

Table 1 Summary of long-term observations used in this study

Network	Location	Period	Resolution	Data sources
AOD				
AVHRR -630nm	Global, ocean	1990-2009*	0.5°×0.5°, Monthly	NOAA's National Climatic Data Center, http://www.ncdc.noaa.gov/cdr/operationalcdrs.html#2
TOMS -500nm	Global, land&ocean	1990-1992, 1996-2001	1°×1°, monthly	http://ozoneaq.gsfc.nasa.gov/aot.md
SeaWiFS -550nm	Global, land&ocean	1998-2010	0.5°×0.5°, Monthly	http://gdata1.sci.gsfc.nasa.gov/daac-bin/G3/gui.cgi?instance_id=SWDB_monthly
MISR -555nm	Global, land&ocean	2000-2010	0.5°×0.5°, Monthly	http://gdata1.sci.gsfc.nasa.gov/daac-bin/G3/gui.cgi?instance_id=MISR_Monthly_L3
MODIS-terra -550nm	Global, land&ocean	2000-2010	1°×1°, Monthly	http://gdata1.sci.gsfc.nasa.gov/daac-bin/G3/gui.cgi?instance_id=MODIS_MONTHLY_L3
MODIS-aqua -550nm	Global, land&ocean	2003-2010	1°×1°, Monthly	
AERONET	Worldwide 693 sites with 11 long-term sites	1992-2010	Monthly	http://aeronet.gsfc.nasa.gov/
Clear-sky SWR				
CERES	Global, land&ocean	2000-2010	1°×1°, Monthly	http://ceres.larc.nasa.gov/
SURFRAD	5 sites in the U.S.	1995-2010	Monthly	Gan et al.(2014)

* Suspiciously high AOD values from AVHRR retrievals in 2001-2002 were not included in this study.

Table 2 Trends in regional AOD from satellite retrievals and WRF-CMAQ model

			Land regions				Ocean regions			
Period	Dataset		ECH	EUS	EUR	SHR	NPA	NAT	CAT	NIN
1990s	AVHRR (1990-2000)		-0.002	-0.006	-0.01	-0.028	-0.002	-0.004	-0.011	-0.018
		%	-0.62	-1.83	-3.37	-3.68	-0.56	-2.41	-2.80	-3.20
		p	-	-	*<0.2*	*<0.1*	-	-	-	-
	TOMS (1990-2001)		-0.002	-0.001	0	-0.009	-0.001	-0.001	-0.006	-0.012
		%	-1.68	-1.30	0.53	-2.35	-0.51	-1.07	-1.42	-3.58
		p	-	-	-	*<0.2*	-	-	-	*<0.2*
	WRF-CMAQ (1990-2000)		0.002	-0.004	-0.007	-0.009	-0.003	-0.004	-0.005	-0.003
		%	0.96	-2.19	-3.52	-2.99	-2.08	-2.53	-1.94	-0.92
		p	<0.05	<0.05	<0.05	<0.1	<0.05	<0.05	<0.1	-
2000s	AVHRR (2000-2009)		0.001	-0.005	-0.005	0.015	-0.005	-0.007	-0.001	0.014
		%	0.358	-1.717	-1.996	2.325	-6.544	-7.489	-0.505	2.81
		p	-	*<0.2*	*<0.2*	-	*<0.05*	*<0.05*	-	*<0.1*
	MODIS-Terra (2000-2010)		0.001	-0.008	-0.007	0	0.001	0	0.002	0.007
		%	0.26	-4.41	-3.84	-0.12	0.31	0.20	0.63	1.08
		p	-	*<0.05*	*<0.05*	-	-	-	-	-
	MODIS-Aqua (2003-2010)		0	-0.007	-0.005	0.002	0.001	-0.001	0	0.008
		%	-0.11	-4.09	-2.64	0.47	0.37	-0.58	-0.04	1.04
		p	-	*<0.1*	*<0.2*	-	-	-	-	-
	SeaWiFS (1998-2010)		0.004	-0.003	-0.002	0.005	0.001	0.001	-0.006	0.014
		%	1.65	-1.47	-1.00	1.12	1.70	0.58	-1.60	2.71
		p	*<0.1*	*<0.05*	*<0.2*	*<0.05*	*<0.05*	-	*<0.05*	*<0.05*
	MISR (2000-2010)		0.002	-0.003	-0.003	0.005	0.002	-0.001	-0.001	0.006
		%	0.86	-1.81	-1.97	1.16	1.26	-0.38	-0.15	1.08
		p	-	*<0.2*	*<0.05*	*<0.2*	*<0.2*	-	-	-
	WRF-CMAQ (2000-2010)		0.014	-0.004	-0.003	0.001	0.003	-0.001	0	-0.003
		%	5.34	-2.66	-2.07	0.33	2.11	-0.67	-0.02	-0.73
		p	<0.05	<0.05	<0.05		<0.05	<0.1		

P-values: the probabilities that the trends are not statistically significant. No values when P>0.2.

Simulation results are all from WRF-CMAQ with feedback; Simulated AOD is reported at local 11:00am for each grid cell;

Table 3 Trends in regional SWR from satellite retrievals and WRF-CMAQ model

			Land regions				Ocean regions			
Period	Dataset		ECH	EUS	EUR	SHR	NPA	NAT	CAT	NIN
(a) Clear-sky upwelling SWR at TOA (W m^{-2})										
1990s	WRF-CMAQ		**0.033**	*-0.082*	*-0.194*	*-0.082*	*-0.092*	*-0.136*	-0.145	-0.113
	(1990-2000)	%	**0.05**	*-0.11*	*-0.27*	*-0.09*	*-0.17*	*-0.25*	-0.26	-0.18
2000s	CERES-EBAF		**0.103**	-0.099	*-0.116*	0.015	0.057	0.023	-0.047	0.016
	(2000-2010)	%	**0.14**	-0.14	*-0.17*	0.01	0.13	0.05	-0.10	0.03
	WRF-CMAQ		**0.301**	*-0.095*	*-0.106*	-0.050	**0.107**	-0.039	-0.040	-0.128
	(2000-2010)	%	**0.42**	*-0.14*	*-0.15*	-0.06	**0.20**	-0.07	-0.07	-0.20
(b) Clear-sky downwelling SWR at surface (W m^{-2})										
1990s	WRF-CMAQ		*-0.124*	**0.182**	**0.414**	0.411	0.129	**0.17**	0.263	0.238
	(1990-2000)	%	*-0.04*	**0.06**	**0.13**	0.13	0.04	**0.05**	0.08	0.08
2000s	CERES-EBAF		*-0.653*	**0.809**	**0.614**	0.268	*-0.344*	-0.081	0.096	-0.010
	(2000-2010)	%	*-0.21*	**0.25**	**0.20**	0.09	*-0.10*	-0.02	0.03	0.00
	WRF-CMAQ		*-0.56*	**0.097**	**0.141**	-0.256	-0.106	0.019	-0.101	0.071
	(2000-2010)	%	*-0.17*	**0.03**	**0.04**	-0.08	-0.03	0.01	-0.03	0.02

* Formatted entries are significant at p=0.05 level: *italic*=significant decrease; **bold**=significant increase.

Simulation results are all from WRF-CMAQ with feedback; simulated SWR is monthly 24 hour average

Table 4 Estimates of 24hour-mean JJA-averaged aerosol direct radiative effect (DRE) and its trends

			Land regions				Ocean regions			
Period	Dataset		ECH	EUS	EUR	SHR	NPA	NAT	CAT	NIN
(a) at TOA										
1990s	DRE	W m^{-2}	-4.9	-4.7	-6.6	-3.0	-5.1	-6.3	-8.3	-10.8
	Trend		*-0.041*	**0.085**	**0.196**	0.061	**0.094**	**0.131**	0.14	0.114
		%	*-0.83*	**1.76**	**2.91**	1.98	**1.81**	**2.02**	1.66	1.02
2000s	DRE	W m^{-2}	-6.5	-3.8	-5.3	-3.1	-5.4	-5.8	-8.1	-11.1
	Trend		*-0.3*	**0.084**	**0.096**	-0.006	*-0.102*	0.034	0.028	0.114
		%	*-4.82*	**2.21**	**1.82**	-0.12	*-1.94*	0.60	0.32	1.05
Yu et al (2006)	DRE	W m^{-2}	-5.0~ -9.4	-5.9~ -11.1	-5.8~ -6.3	-4.9~ -9.0	-5.7~ -12.7	-4.4~ -8.7	-5.7~ -12.8	-8.5~ -17.5
(b) at surface										
1990s	DRE	W m^{-2}	-9.9	-9.4	-13.1	-17.7	-7.3	-9.5	-14.6	-18.9
	Trend		-0.07	**0.161**	**0.4**	0.483	**0.147**	**0.213**	0.292	0.231
		%	-0.70	**1.62**	**2.99**	2.64	**1.97**	**2.16**	1.96	1.21
2000s	DRE	W m^{-2}	-13.0	-7.7	-10.6	-18.8	-7.8	-8.7	-14.7	-18.8
	Trend		*-0.558*	**0.157**	**0.193**	-0.037	*-0.149*	0.052	0.004	0.186
		%	*-4.46*	**2.02**	**1.84**	-0.08	*-1.97*	0.61	0.00	1.03

* Formatted entries are significant at p=0.05 level: *italic*=significant decrease; **bold**=significant increase.

The regions defined in Yu et al (2006) are slightly different as this study, with ECH compared to land in zines 4&8 of Yu et al. (2006), EUS to land in zone 2, EUR to land in zone 3, SHR to land in zone 7, NPA to ocean in zones 1 & 4, NAT to ocean in zone 2, CAT to ocean in zone 6, and NIN to ocean in zone 7.

Table 5 Estimates of summertime aerosol direct radiative efficiency (E_τ, $Wm^{-2}\ \tau^{-1}$) averaged for 2000-2010

		Land regions				Ocean regions			
		ECH	EUS	EUR	SHR	NPA	NAT	CAT	NIN
AOD	Obs.	0.34	0.19	0.17	0.45	0.14	0.14	0.36	0.56
	Sim. (at noon)	0.27	0.14	0.15	0.30	0.14	0.15	0.27	0.36
	Sim. (24h-mean)	0.14	0.08	0.09	0.16	0.08	0.09	0.14	0.19
(a) at TOA									
$E_{\tau\text{-}yu}$	Obs.	-9~-33	-24~-37	-11~-34	-	-18~-52	-30~-60	-18~-52	-23~-45
$E_{\tau\text{-}yu}$	Sim.	-19~-27	-21~-37	-13~-26	-	-25~-42	-27~-42	-16~-41	-14~-37
E_τ	Sim.	-45.4	-49.6	-57.2	-19.3	-66.9	-65.3	-56.7	-57.0
E_τ^*	Sim.	-42.0	-48.8	-55.4	-9.8	-60.9	-59.2	-52.1	-59.5
$E_{\tau 2}^*$	Obs.	-7.65	-8.72	-15.42	-3.28	-22.92	-19.45	-8.55	-7.26
		R(0.61)	R(0.37)	R(0.59)	R(0.36)	R(0.70)	R(0.75)	R(0.69)	R(0.63)
	Sim.-feedback	-22.21	-25.17	-32.46	-6.25	-36.15	-33.23	-25.96	-27.63
		R(0.99)	R(0.90)	R(0.93)	R(0.77)	R(0.96)	R(0.91)	R(0.98)	R(0.96)
	Sim.-no feedback	-0.03	-2.73	-4.84	-0.02	-0.80	-0.56	-0.96	-0.45
		R(0.01)	R(0.28)	R(0.36)	R(0.00)	R(0.12)	R(0.05)	R(0.48)	R(0.18)
(b) at surface									
$E_{\tau\text{-}yu}$	Obs.	-51~-82	-65~-84	-57~-98	-	-61~-90	-67~-90	-65~-78	-58~-86
$E_{\tau\text{-}yu}$	Sim.	-40~-54	-38~-66	-36~-68	-	-45~-61	-42~-76	-27~-68	-34~-77
E_τ	Sim.	-90.8	-101.5	-114.3	-116.1	-96.9	-98.7	-103.1	-96.8
E_τ^*	Sim.	-78.2	-44.6	-88.2	-106.3	-68.8	-59.2	-79.8	-79.6
$E_{\tau 2}^*$	Obs.	-47.59	-79.45	-69.56	-22.60	-50.25	-41.65	-19.00	-13.36
		R(0.76)	R(0.68)	R(0.66)	R(0.40)	R(0.65)	R(0.56)	R(0.63)	R(0.67)
	Sim.-feedback	-41.41	-32.09	-66.41	-56.00	-47.79	-60.71	-50.39	-51.61
		R(0.96)	R(0.54)	R(0.67)	R(0.96)	R(0.68)	R(0.49)	R(0.95)	R(0.97)
	Sim.-no feedback	-0.16	14.97	3.31	0.04	6.68	-7.05	8.44	2.90
		R(-0.01)	R(0.26)	R(0.05)	R(0.00)	R(0.12)	R(-0.07)	R(0.44)	R(0.16)

AOD is averaged for 2000-2010;

E_τ is calculated by using DRE divided by AOD;

E_τ^* is the slope of DRE against AOD;

$E_{\tau 2}^*$ is calculated by deseasonalized SWR and AOD, observed SWR is from CERES, observed AOD is the weighted average of 4 EOS satellites retrievals by available number of grids for calculation, see Fig. 3; correlation coefficients (R) between SWR and AOD are calculated and shown in brackets for obs., sim.-feedback and –no feedback case;

$E_{\tau\text{-}yu}$ is the data reported in Yu et al (2006) which summarized both measurement-based and GCM estimations;

The regions defined in Yu et al (2006) are slightly different as this study, with ECH compared to land in zines 4&8 of Yu et al. (2006), EUS to land in zone 2, EUR to land in zone 3, SHR to land in zone 7, NPA to ocean in zones 1 & 4, NAT to ocean in zone 2, CAT to ocean in zone 6, and NIN to ocean in zone 7.

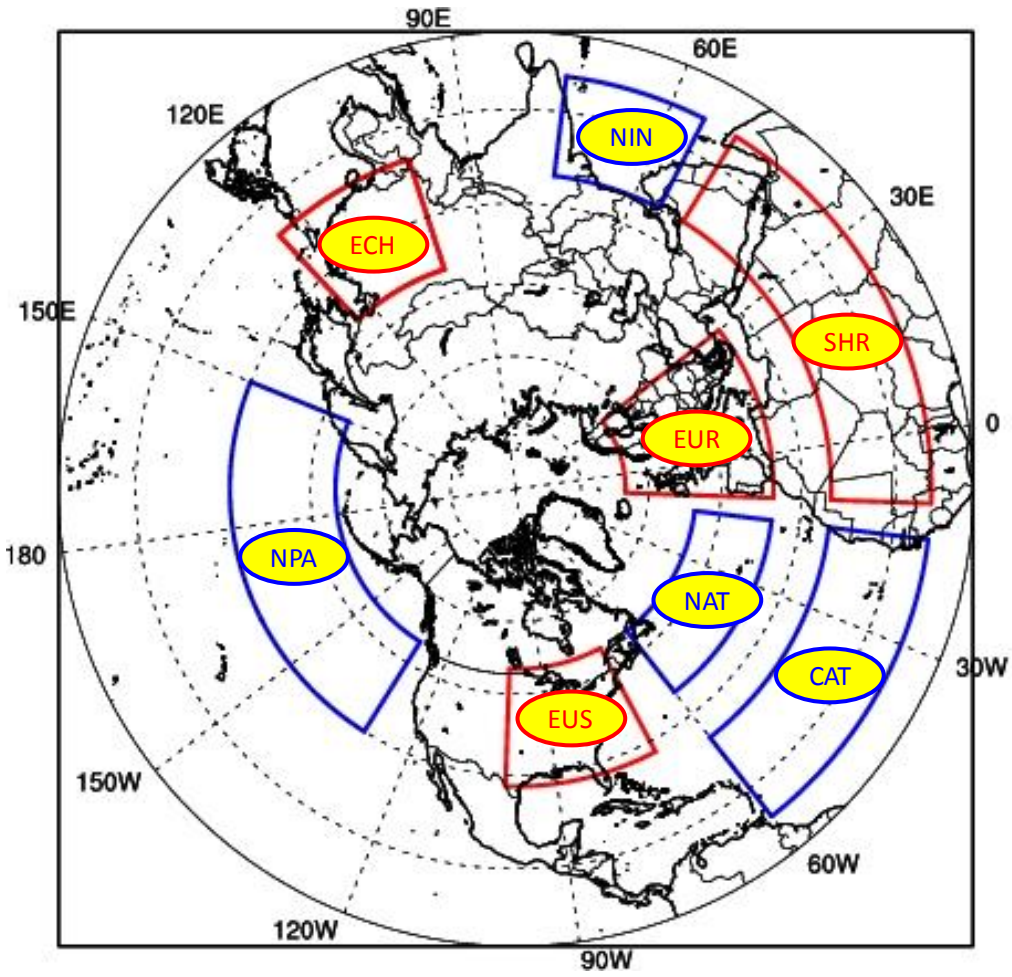

Fig. 1 Simulation domain and targeted regions

*Land regions: Eastern China (ECH, 20N-40N, 100E-125E), Eastern US (EUS, 28N-50N,100W-70W), Europe (EUR, 35N-65N, 10W-30E) and Sahara Desert (SHR, 10N-25N, 10W-50E);

Ocean regions: North Pacific (NPA, 30N-50N, 150E-130W), North Atlantic (NAT, 35N-50N, 60W-15W); Central Atlantic (CAT, 10N-25N, 60W-15W); North Indian Ocean (NIN, 10N-25N, 55E-75E).

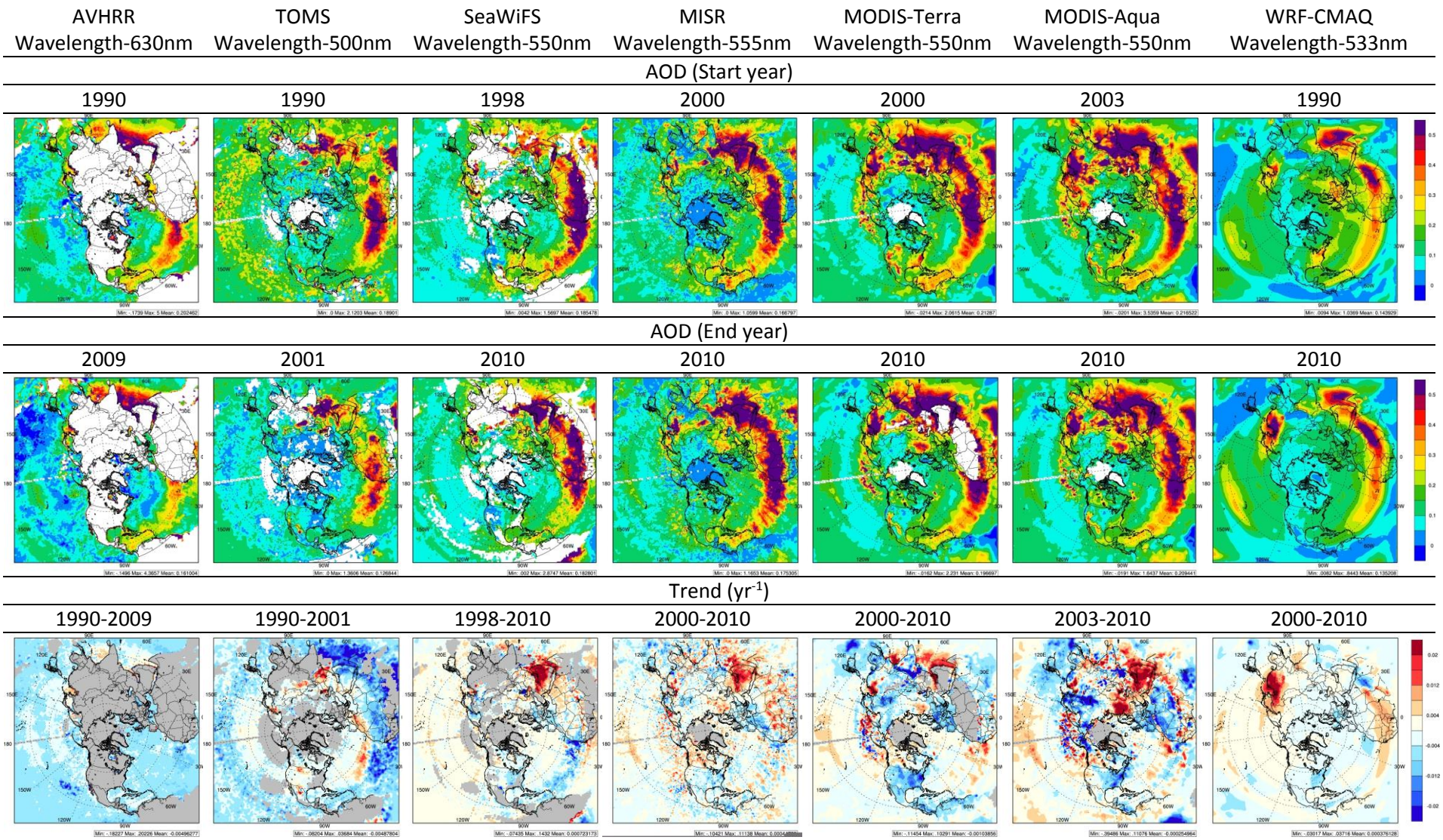

Fig. 2 Spatial distribution of summertime AOD and its trend from satellite retrievals and WRF-CMAQ model

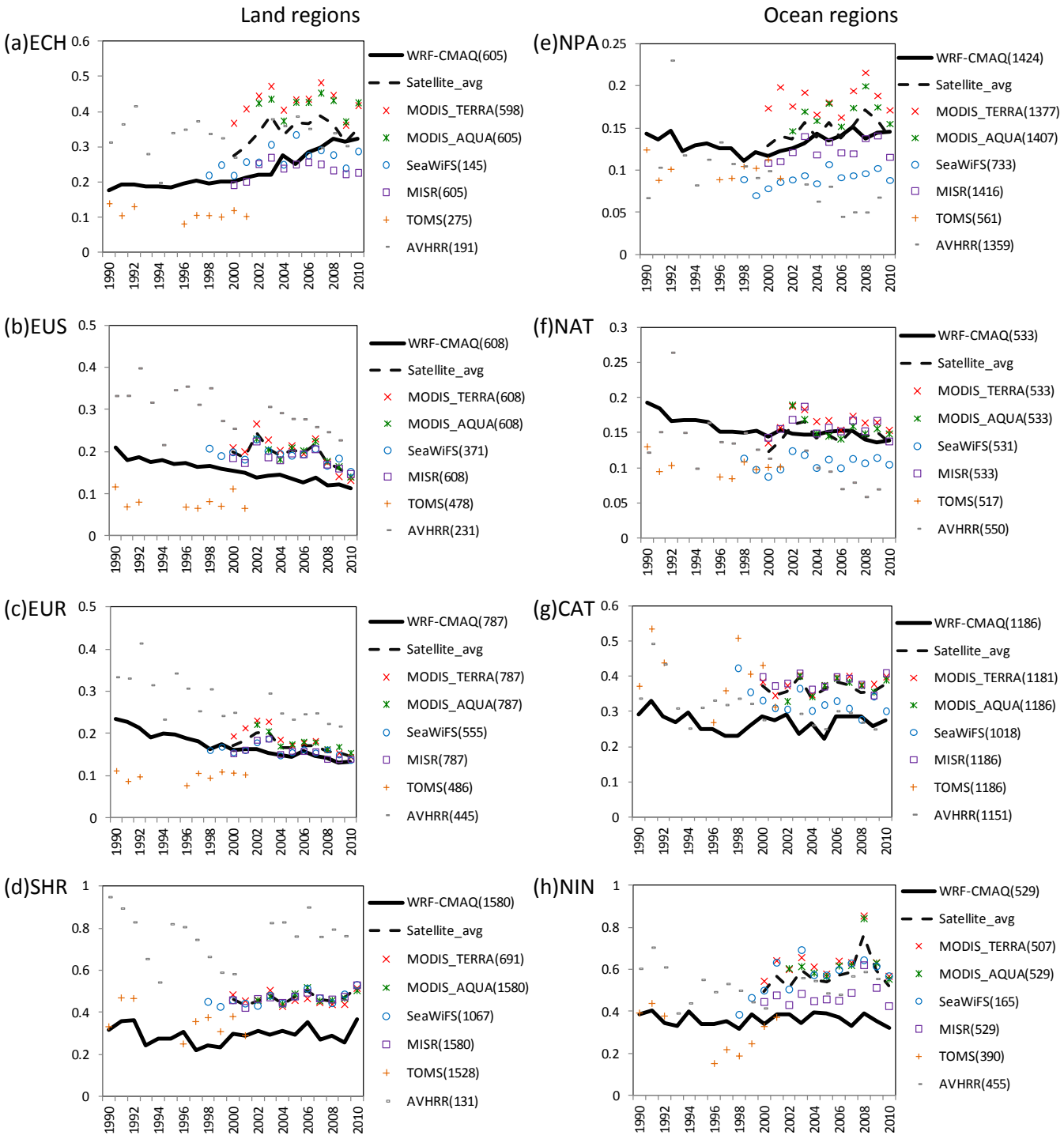

Fig. 3 Temporal series of regional JJA-averaged AOD from satellite retrievals and WRF-CMAQ

Number of grids (> 80% coverage) involved in calculation is shown in the bracket; only 4 EOS satellite-retrieved AODs, i.e., MISR, SeaWiFS, MODIS-terra and –aqua, were averaged into "Satellite-avg"

(a) AERONET

(b) WRF-CMAQ

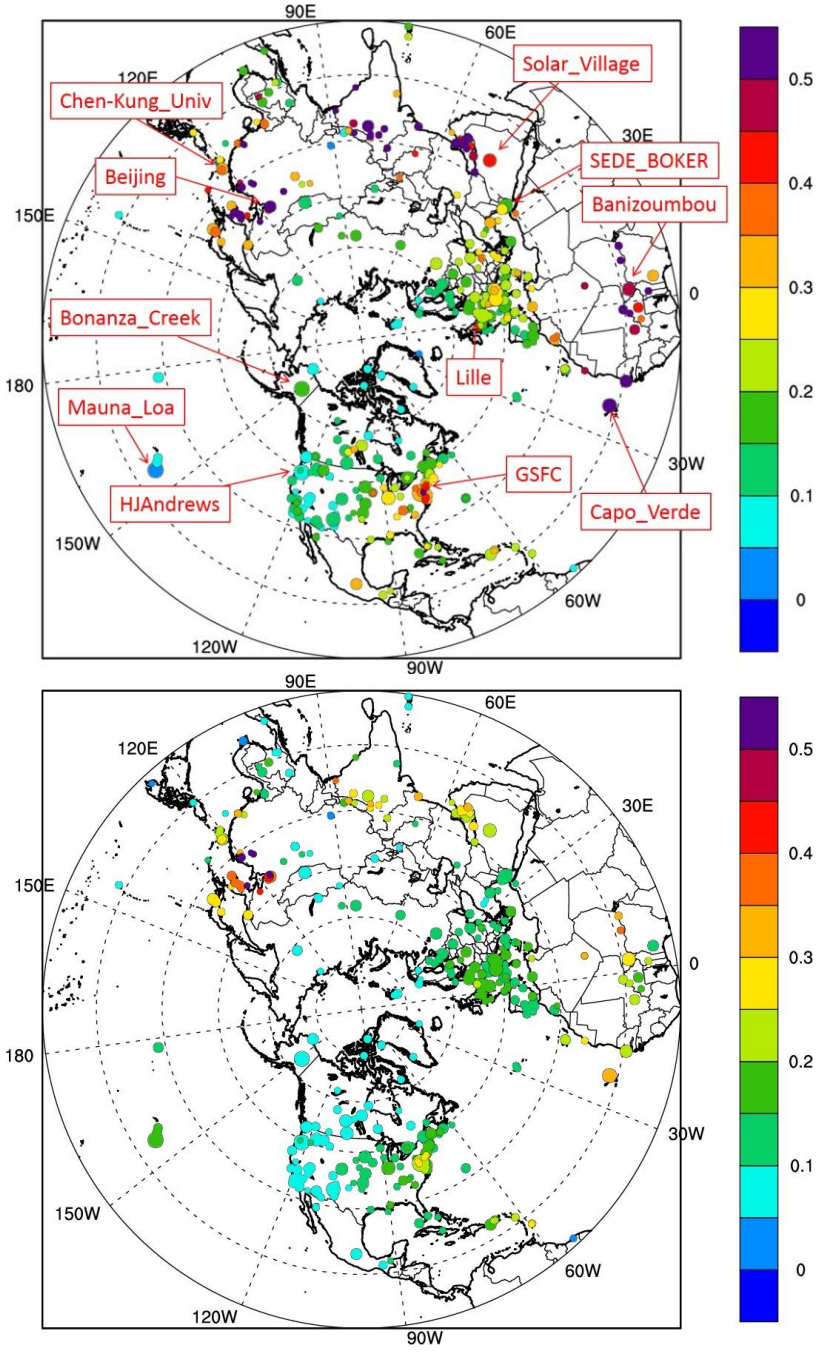

Fig. 4 Comparison of spatial distributions of summer AOD between AERONET and WRF-CMAQ (dot size indicates the extent of data coverage for the period 1990-2010; all converted into 533nm; sites marked by red boxes are selected for trend analysis)

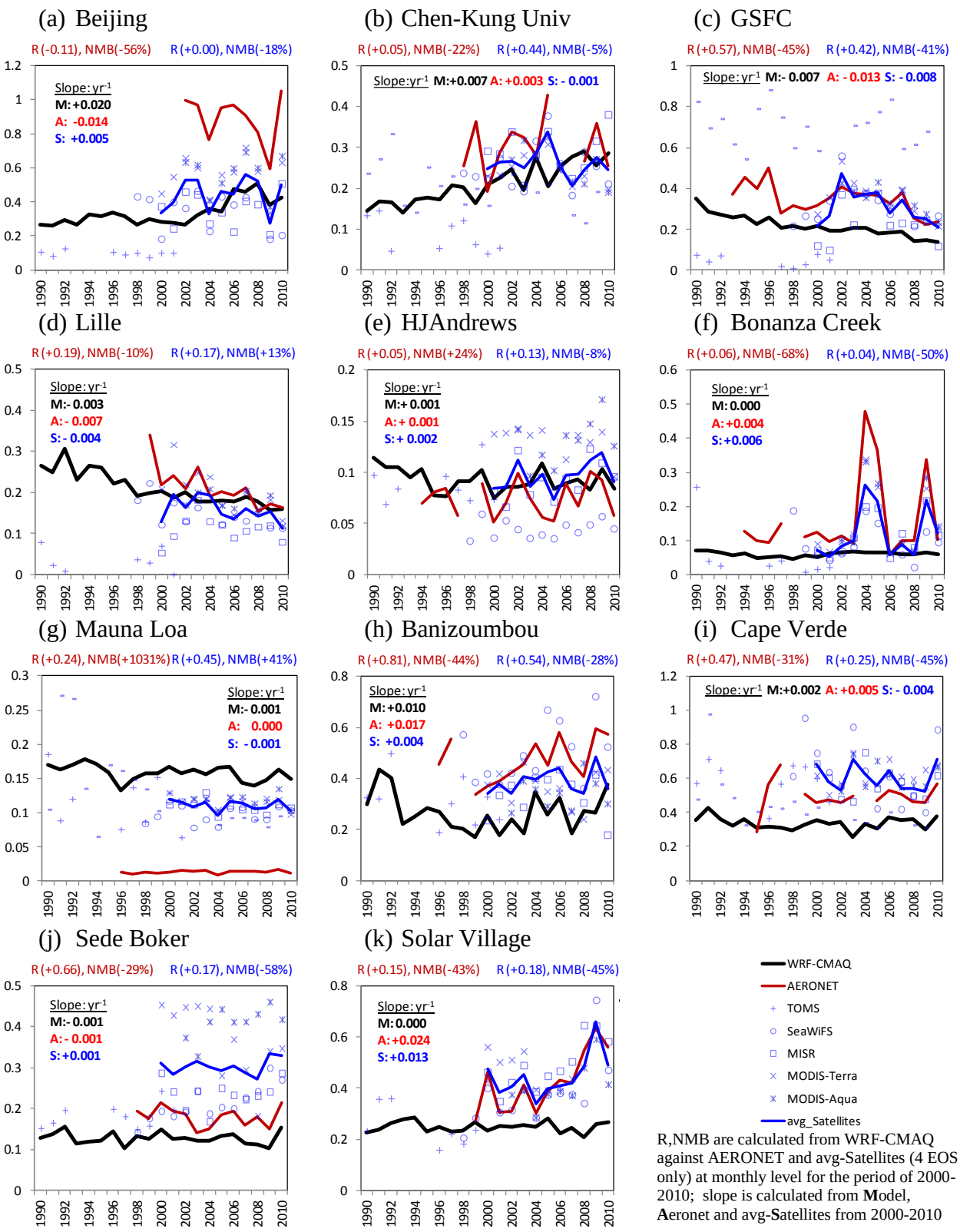

R,NMB are calculated from WRF-CMAQ against AERONET and avg-Satellites (4 EOS only) at monthly level for the period of 2000-2010; slope is calculated from **M**odel, **A**eronet and avg-**S**atellites from 2000-2010

Fig. 5 Comparison of JJA-averaged AOD of selected AERONET sites

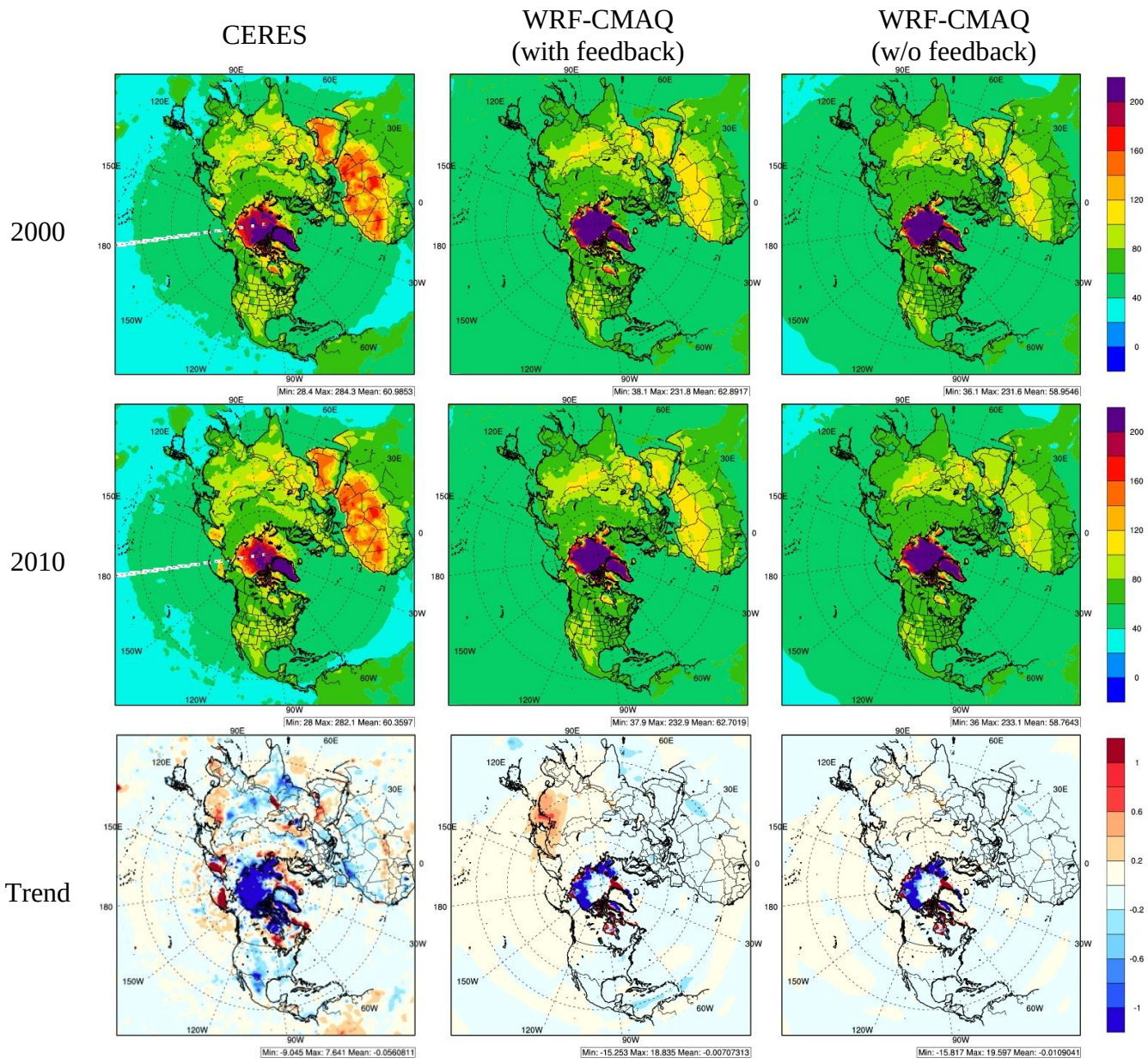
CERES
WRF-CMAQ
(with feedback)
WRF-CMAQ
(w/o feedback)
2000
2010
Trend
Min: 28.4 Max: 284.3 Mean: 60.9853
Min: 38.1 Max: 231.8 Mean: 62.8917
Min: 36.1 Max: 231.6 Mean: 58.9546
Min: 28 Max: 282.1 Mean: 60.3597
Min: 37.9 Max: 232.9 Mean: 62.7019
Min: 36 Max: 233.1 Mean: 58.7643
Min: -9.045 Max: 7.641 Mean: -0.0560811
Min: -15.253 Max: 18.835 Mean: -0.00707313
Min: -15.817 Max: 19.597 Mean: -0.0109041

(a)

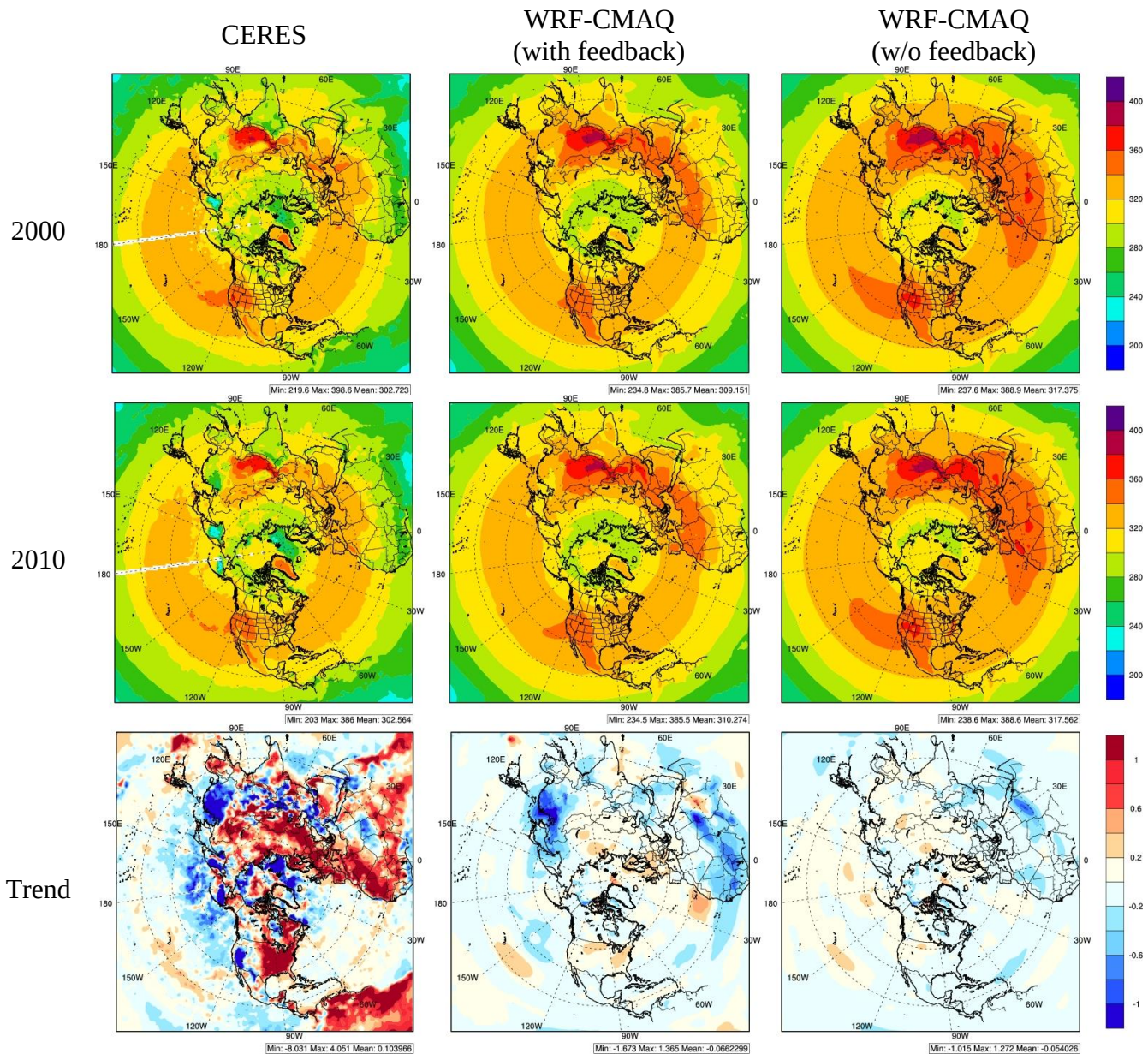

(b)

Fig. 6 Spatial distribution of summertime clear-sky shortwave radiation (SWR) from CERES satellite and WRF-CMAQ model: (a) at TOA (upwelling), (b) at surface (downwelling)

(unit: W m^{-2}, trends are computed on the basis of JJA-average over the 2000-2010 period with a linear least square fit method)

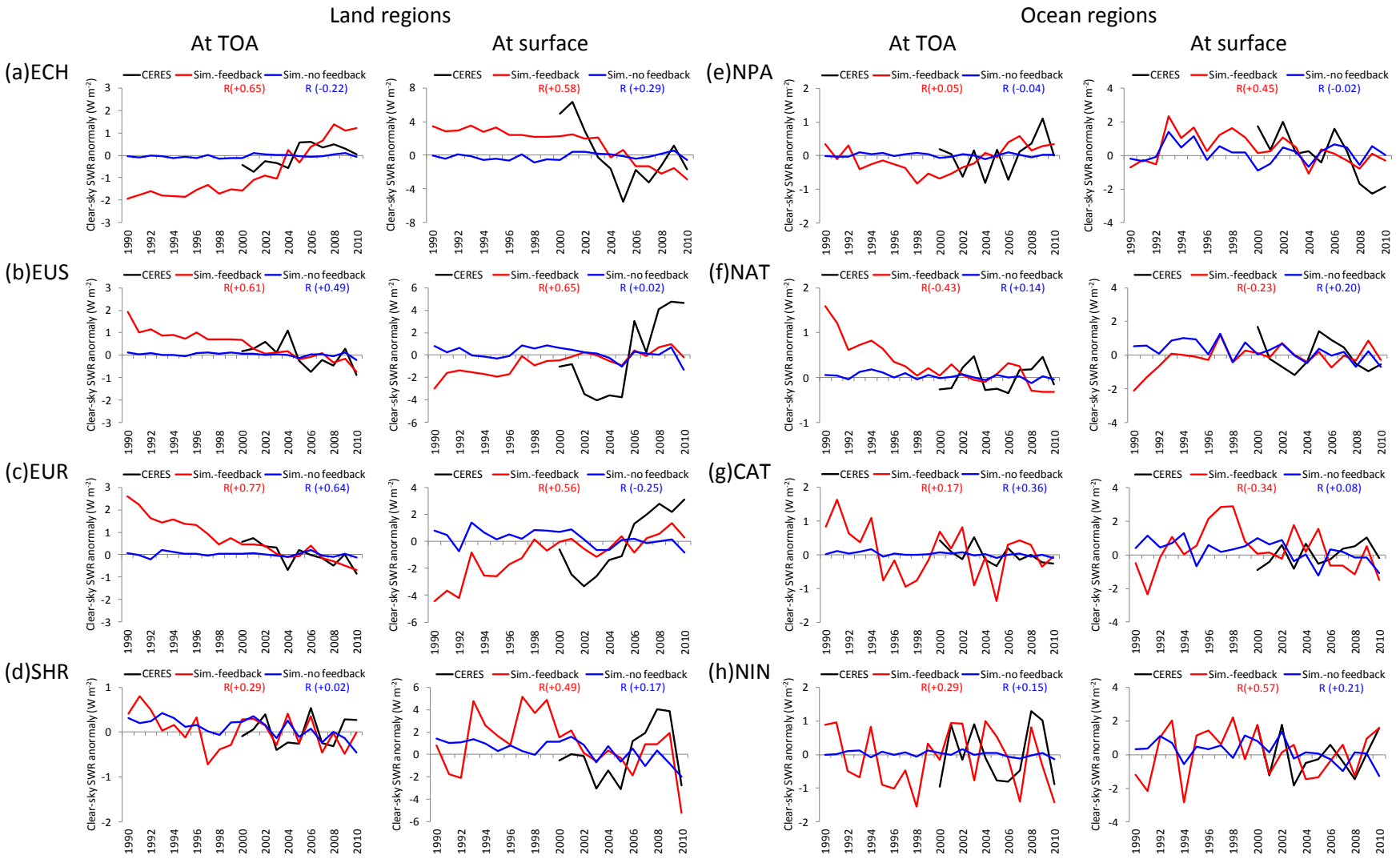

Fig. 7 Observed and simulated time-series of summertime clear-sky SWR at TOA and surface (regional JJA-average, anomaly to the average of 2000-2010; R is calculated from Sim.-feedback and Sim.-no feedback against with CERES)

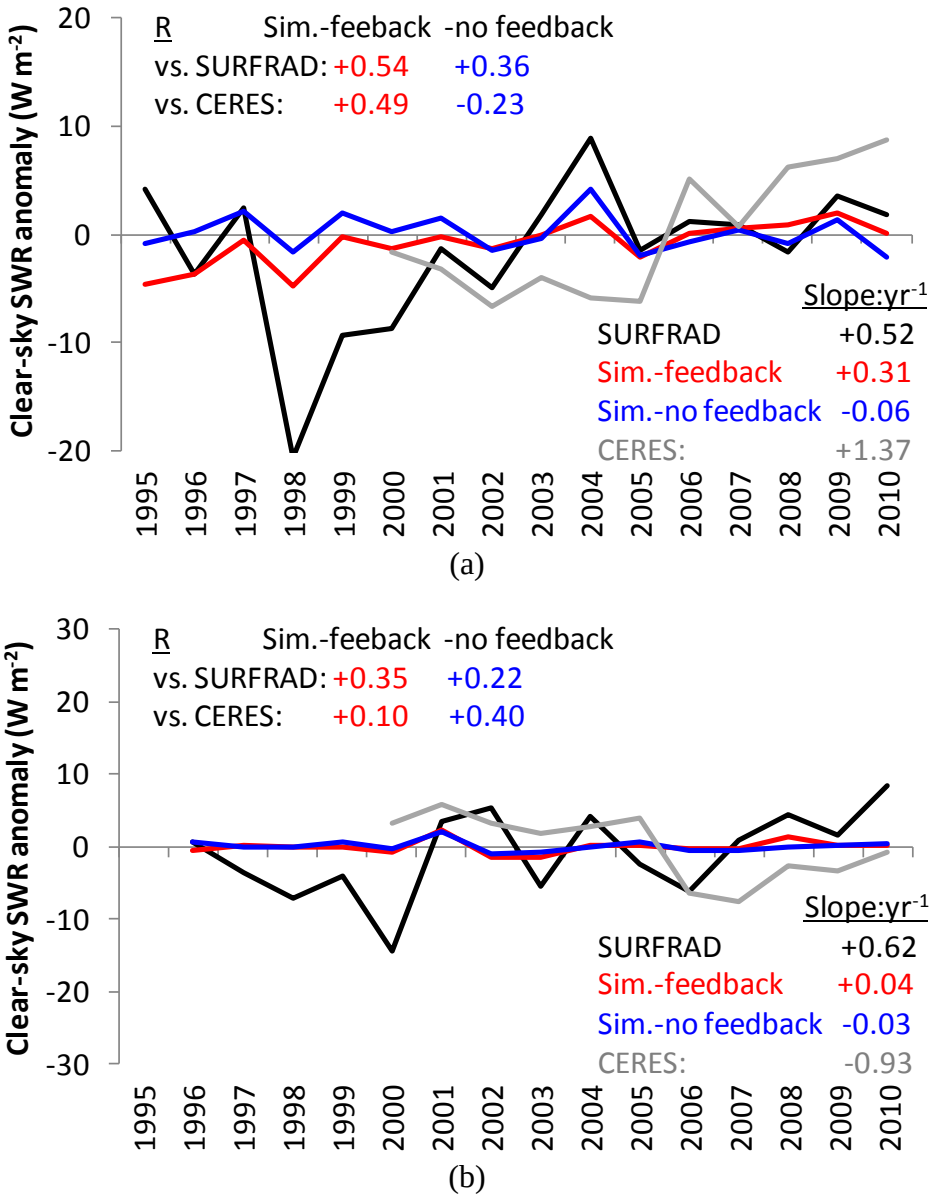

Fig. 8 Comparison of SURFRAD/Ceres observed and WRF-CMAQ clear-sky SWR at the surface: (a) the eastern U.S. (b) the western U.S.
(site-averaged, anomaly to the average of 1995-2010)

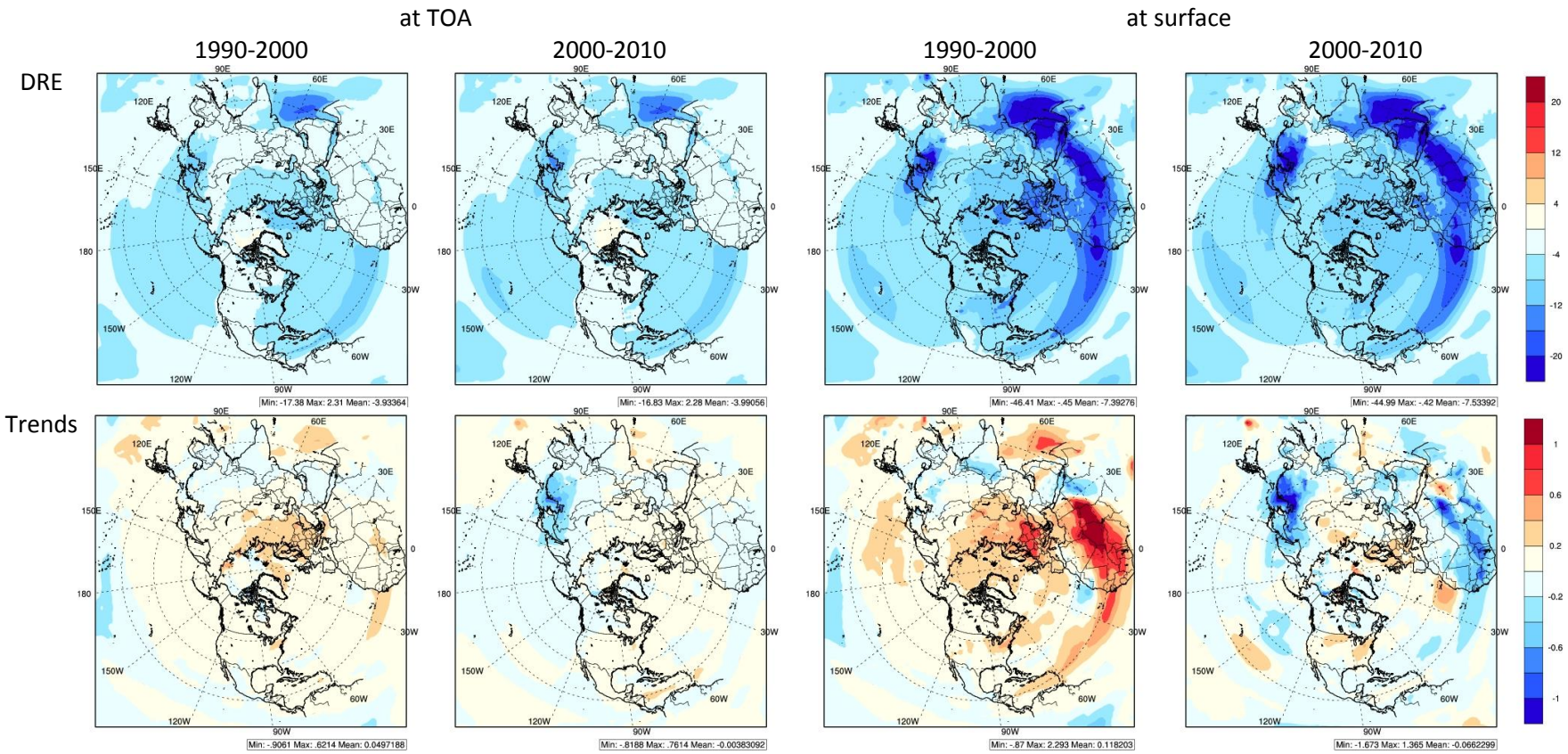

Fig. 9 spatial distributions of simulated DRE and its trends (W m^{-2})

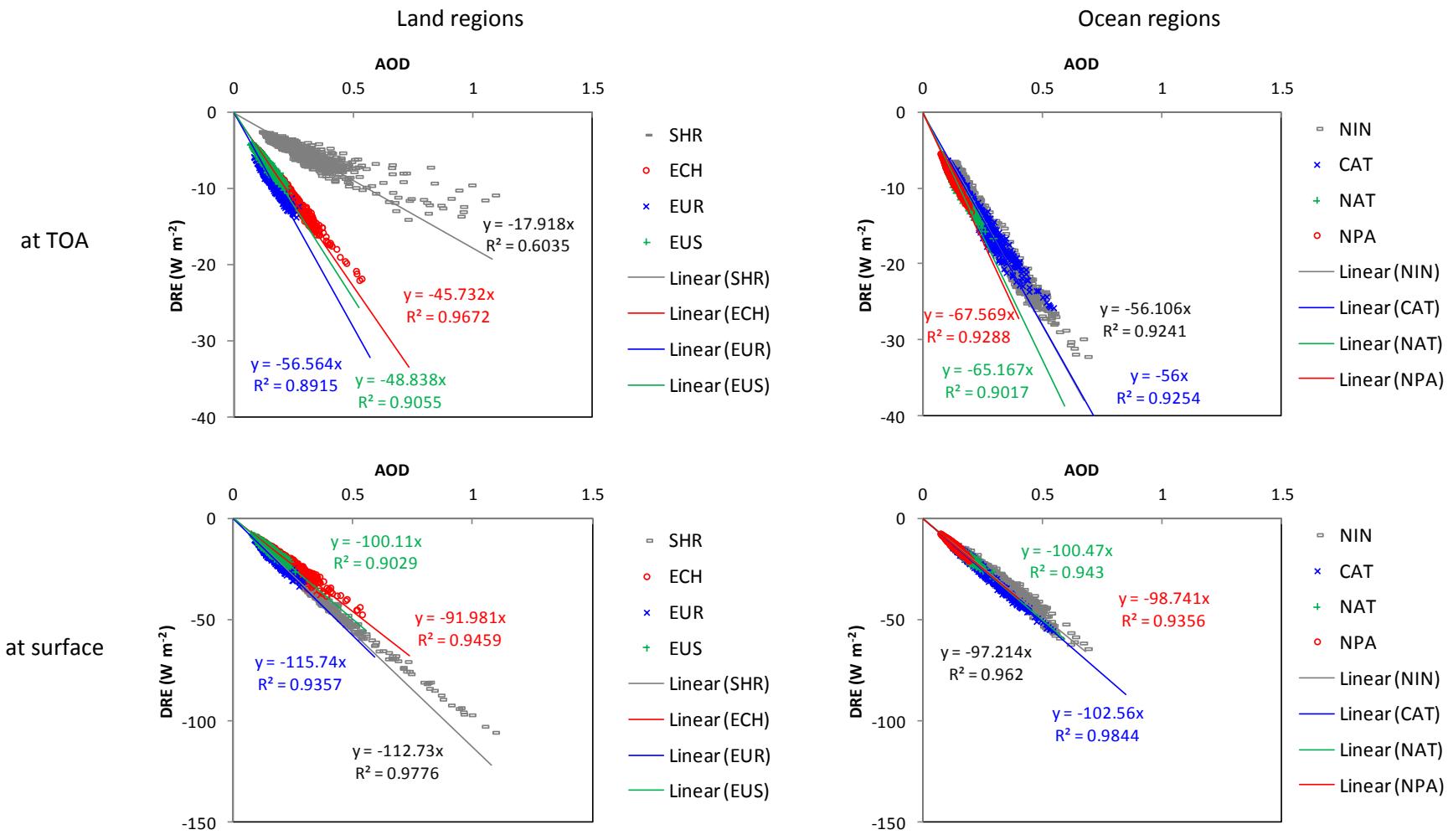

Fig. 10 Daily daytime clear-sky DRE against AOD (local time 6:00-20:00 averaged regionally and temporally over 1990-2010)